Materials Today Bio 18 (2023) 100500

Contents lists available at ScienceDirect

Materials Today Bio

journal homepage: www.journals.elsevier.com/materials-today-bio

Bioactive graphene oxide-functionalized self-expandable hydrophilic and osteogenic nanocomposite for orthopaedic applications

Quan-Chang Tan [a,b,1], Xia-Shu Jiang [c,1], Lei Chen [c,1], Jin-Feng Huang [a], Qiu-Xia Zhou [c], Jing Wang [a], Yan Zhao [a], Bo Zhang [c], Ya-Ni Sun [c], Min Wei [c], Xiong Zhao [a], Zhao Yang [a], Wei Lei [a,*], Yu-Fei Tang [c,**], Zi-Xiang Wu [a,***]

[a] Department of Orthopaedics, Xijing Hospital, The Air Force Medical University, Changlexi Road No. 127, Xi'an, Shaanxi Province, PR China
[b] Department of Orthopaedics, Air Force Hospital of Eastern Theater Command, Malujie Road No. 1, Nanjing, Jiangsu Province, PR China
[c] School of Materials Science and Engineering, The Xi'an University of Technology, No. 5 Jinhua South Road, Xi'an, Shaanxi Province, PR China

ARTICLE INFO

Keywords:
Expandable material
Graphene oxide
Water absorption
Biomechanics
Osteointegration

ABSTRACT

Polymethyl methacrylate (PMMA) bone cement (PBC) is commonly used in orthopaedic surgery. However, polymerization volumetric shrinkage, exothermic injury, and low bioactivity prevent PBC from being an ideal material. The developed expandable P(MMA-AA-St) well overcomes the volumetric shrinkage of PBC. However, its biomechanical properties are unsatisfactory. Herein, graphene oxide (GO), a hydrophilic material with favourable biomechanics and osteogenic capability, was added to P(MMA-AA-St) to optimize its biomechanics and bioactivity. The GO-modified self-expandable P(MMA-AA-St)-GO nanocomposite (PGBCs) exhibited outstanding compressive strength (>70 MPa), water absorption, and volume expansion, as well as a longer handling time and a reduced setting temperature. The cytocompatibility of PGBCs was superior to that of PBC, as demonstrated by CCK-8 assay, live-dead cell staining, and flow cytometry. In addition, better osteoblast attachment was observed, which could be attributed to the effects of GO. The improved level of osteogenic gene and protein expression further illustrated the improved cell-material interactions between osteoblasts and PGBCs. The results of an *in vivo* study performed by filling bone defects in the femoral condyles of rabbits with PGBCs demonstrated promising intraoperative handling properties and convenient implantation. Blood testing and histological staining demonstrated satisfactory *in vivo* biosafety. Furthermore, bone morphological and microarchitecture analyses using bone tissue staining and micro-CT scanning revealed better bone-PGBCs contact and osteogenic capability. The results of this study indicate that GO modification improved the physiochemical properties, cytocompatibility, and osteogenic capability of P(MMA-AA-St) and overcame the drawbacks of PBC, allowing its material derivatives to serve as effective implantable biomaterials.

1. Introduction

Polymethyl methacrylate (PMMA) bone cement (PBC) is a conventional orthopaedic biomaterial that can function as a prosthetic fixator, a bone filler, and an antibiotic carrier in arthroplasty and spinal and emergency surgery due to its chemical inertness and facile manipulation [1–5]. However, the volumetric shrinkage, high elastic modulus, toxification, and poor osteointegration of PBC are still concerns regarding its clinical application.

The volumetric shrinkage resulting from polymerization is a drawback of PBC [6]. The theoretical shrinkage rate was estimated to be up to 21%, and the experimentally verified shrinkage rate was found to be 3.82–10.5% [7–9]. Two mechanisms are responsible for this shrinkage and the resulting stress formation: (i) the increase in pure density due to the polymerization of the initial monomer into the final polymer; and (ii) the increase in thermal shrinkage due to the contraction of PBC upon

* Corresponding author. Department of Orthopaedics, Xijing Hospital, No. 127 Changlexi Road, Xi'an Shaanxi Province, 710032, PR China.
** Corresponding author. School of Materials Science and Engineering, Xi'an University of Technology, No. 5 Jinhua South Road, Xi'an, Shaanxi Province, 710048, PR China.
*** Corresponding author. Department of Orthopaedics, Xijing Hospital, No. 127 Changlexi Road, Xi'an, Shaanxi Province, 710032, PR China.
E-mail addresses: leiwei@fmmu.edu.cn (W. Lei), yftang@xaut.edu.cn (Y.-F. Tang), wuzixiang@fmmu.edu.cn (Z.-X. Wu).
[1] These authors have contributed equally to this work.

https://doi.org/10.1016/j.mtbio.2022.100500
Received 11 August 2022; Received in revised form 30 October 2022; Accepted 18 November 2022
Available online 23 November 2022

cooling [10]. This polymerization-related shrinkage and strain has been reported to be an important factor influencing the biomechanics and interfacial integrity between the composite and anchor base because shrinkage could destroy the interdigitation of the cement in trabecular bone [11]. Consequently, volumetric shrinkage resulting in a cement-bone interfacial gap is regarded as one of the main causes of failure in vertebral augmentation and joint replacement [12–14].

Despite the sufficient compressive strength of PBC, its high elastic modulus has been found to compromise its overall biomechanical advantages. This defect has been reported to be responsible for adjacent vertebral fracture after vertebroplasty due to changes in load transfer [15]. Therefore, many additive materials, such as collagen [16], linoleic acid [17], poly (butyl acrylate) [17], and hyaluronic acid [18], have been introduced into PBC to reduce its elastic modulus.

Besides, toxicity is one biological concern related to the clinical use of PBC. The toxicity of PBC has been reported to be generated mainly from residual radicals and unpolymerized monomers, which impair the viability of osteoblasts [19]. Additionly, monomers are thought to be one of the causes of bone cement implantation syndrome (BCIS) in clinical applications, which is a severe perioperative complication characterized by hypoxia, arterial and pulmonary hypertension, and even death [20,21]. Therefore, many alternative methods have been introduced to scavenge radicals, such as the addition of antioxidants such as *N*-acetyl cysteine and methionine [22–24] and the replacement of benzoyl peroxide (BPO) as the polymerization initiator by tri-*n*-butyl borane to reduce free radical production [25,26]. Moreover, hydrophilic substances, such as hydroxyethyl methacrylate, have been applied to partially replace and thus reduce the total amount of MMA monomer [26,27].

While osteointegration is another biological concern in the application of PBC, which refers to the capability of bone tissue to form around a material. PBC is a well-known bioinert material without the capability for osteointegration. The incorporation of a bioactive substance to enhance the bioactivity of another material is a common technique in the development of biomaterials. Therefore, chitosan, bioactive ceramics, and graphene-based materials have been doped into PBC to enhance its osteogenic capability [28–31], and the proliferation, adhesion, spreading, and osteogenic gene expression of osteoblasts have been reported to be significantly improved after this modification [30]. However, the biomechanical impairment that is likely to result from directly incorporating these substances into PBC is a disadvantage of this method of modification, which might be correlated with enhanced brittleness and the aggregation or degradation of additive particles [31–34].

To counteract the volumetric shrinkage of PBC, a PMMA-based expandable bone cement P(MMA-AA-St) was investigated in our previous work [35]. P(MMA-AA-St) is a copolymer of methyl methacrylate (MMA), acrylic acid (AA), and styrene (St) with a 3D network structure, in which AA is a hydrophilic group that absorbs water, while St is a mechanically stronger group that enhances biomechanical properties. Because of the remarkable water absorption capability resulting from the incorporation of AA and its network structure, 87.5% volume expansion could be achieved to overcome the volumetric shrinkage of PBC. In addition, P(MMA-AA-St) possessed better biocompatibility than PBC due to its hydrophilicity after AA incorporation. This improvement was in accordance with previous findings detected after the hydrophilic modification of PBC [26,27]. The water uptake markedly resolved the volumetric shrinkage but affected the biomechanical properties of PBC. Despite the reinforcement of P(MMA-AA-St) by St, its compressive strength was 58.9 MPa, which did not meet the ISO requirement for bone cement (70 MPa) [23].

Graphene oxide (GO), a one-atom-thick 2D layer with distinct physicochemical features, such as hydrophilicity, a honeycomb carbon lattice, and various surface functional groups (-C-O-C, –OH, –COOH), has been widely investigated in the biomedical field. In the field of bone regeneration, GO has been found to facilitate the attachment, proliferation, and osteogenic differentiation of mesenchymal stem cells [36]. Additionally, via mechanisms of cell growth and differentiation regulation, GO enriches cellular stimulus agents [36,37], affects cellular morphology [38], and upregulates differentiation-related signal transduction [39]. In addition, GO improves the biomechanical properties of the materials it is used to modify. GO-containing 3D scaffolds, hydrogel fibres, and ceramics exhibit superior biomechanics compared to their GO-free counterparts. The intrinsic strength and strong interactions of GO, such as hydrogen bonding between base materials and GO, have been reported to be responsible for the improved biomechanics observed after the GO modifications mentioned above [40–42].

GO and its functionalized products have already been employed, alone or accompanied by other inorganic materials, to reinforce PBC and thereby improve its biological properties. Paz and colleagues discovered that the bending and compressive strength, fracture toughness, fatigue properties, and thermal properties were all optimized by introducing no more than 1 wt% GO into PBC. They also found that GO was more effective than graphene in enhancing the biomechanical properties of PBC, which was attributed to the surface of GO presenting a higher quantity of functional groups (e.g. –OH, –COOH) that could facilitate to create of a stronger interfacial adhesion between GO and PBC [43]. Similar findings were also observed by Gonçalves when comparing GO to carbon nanotubes for the reinforcement of PBC due to GO possessing a high specific area and wrinkled surface, which can achieve better GO-PBC integration and high matrix adhesion/interlocking [44]. Furthermore, the biocompatibility of PBC was improved after GO modification, and the surface mineralization, cell viability, and osteogenic gene expression were all optimized after GO modification [31,45].

In this study, GO was applied to further optimize the biomechanics and osteogenic capability of P(MMA-AA-St). Two methods, synthesizing GO with MMA, AA, and St to form a P(MMA-AA-St)-GO nanocomposite and mixing GO with P(MMA-AA-St) nanoparticles, were adopted to incorporate GO to optimize P(MMA-AA-St). Thereafter, the optimal method of incorporating GO was determined by evaluating the physicochemical properties, *in vitro* and *in vivo* biocompatibility, and osteointegration of the products. There are previously reported studies that mixed GO nanosheet into PBC to optimize its physicochemical properties [31,43–46]. The novelty of the present study concluded as follows: (1) GO was applied to optimize the physiochemical properties of P(MMA-AA-St) while improving its capacity of water uptake and volume expansion but preserving adequated biomechanics; (2) the improvement of biocompatibility, osteogenesis, and biosafety of GO modification was proved by *in vitro* and *in vivo* studies due to the *in vivo* investigation is a crucial step for clinical translation; (3) synthesizing might be superior to traditional mixing in acrylic bone cement optimization.

2. Material and methods

2.1. Material fabrication

2.1.1. P(MMA-AA-St)-GO synthesis

The P(MMA-AA-St)-GO copolymer was synthesized using dispersion polymerization. The monomers MMA, AA, and St (all from Kermel, Tianjin, China) were continuously stirred with ultra-sonication to form a homogeneous solution at a 1:1:1 M ratio in a three-necked flask under nitrogen, followed by the sequential addition of a solution of polyvinylpyrrolidone (PVP, Sigma–Aldrich, Shanghai, China) as the dispersing agent (predissolved in deionized water), *N*,*N*′-methylenebisacrylamide (MBA, Damao, Tianjin, China) as the cross-linking agent (predissolved in deionized water), 2,2-azobis (2-methylpropionitrile) (AIBN, Adamas, Shanghai, China) as the initiator (predissolved in anhydrous ethanol) and GO (Sigma–Aldrich, Shanghai, China) suspension (predispersed in deionized water). The ratios of PVP, MBA, AIBN, and GO addition were 8 wt%, 5 wt%, 2 wt%, and 0.5 wt% of the monomers, respectively. The reaction solution was a mixture of deionized water and anhydrous ethanol at a volume ratio of 4:1 (including the volume of predissolved PVP, MBA, and AIBN, and predispersed GO, Fig. S1). The crude product was obtained after polymerization in a water

bath with mechanical agitation (60 rpm) using a motor agitator (Lichen-bx instrument, Shanghai, China) at 70 °C for 3 h under nitrogen, and the obtained product was washed with deionized water ten times to remove residuals, filtered, and freeze-dried to obtain the grey P(MMA-AA-St)-GO copolymer (Fig. S2). Then, the P(MMA-AA-St)-GO copolymer was milled in a ball mill (QM-3SP2, Nanda instrument, Jiangsu, China) for 3 h into a powder.

The procedure for synthesizing P(MMA-AA-St), including the amount and ratio of reagents and the reaction conditions, was the same as those for synthesizing P(MMA-AA-St)-GO except without the GO dispersion. The polymerized reaction of P(MMA-AA-St) was illustrated in Fig. S3.

2.1.2. Bone cement preparation

A: **PMMA bone cement (PBC)**: Commercial PBC (Mendec® Spine 1230, Tecres S.p.A., Italy), which is a product for vertebroplasty and had been used in the study of PBC optimization [47,48] , was used as the control in the present study. According to the manufacturer's instruction, a package of Mendec® Spine consists of a solid phase (20 g) and a liquid phase (10 mL). The $BaSO_4$ was mixed in the solid phase as the X-ray contrast agent by the manufacturer. The PBC was manipulated according to the manufacturer's instructions.

B: **P(MMA-AA-St) synthesized with GO bone cement** (**PGBCs**, in which s means synthesis): P(MMA-AA-St)-GO and commercial PBC powder (Mendec® Spine) were mixed in a ball mill at a volume ratio of 1:1 and milled for 24 h to obtain the PGBCs solid phase. The X-ray contrast agent of PGBCs was the $BaSO_4$ originated from the PBC powder and no additional $BaSO_4$ was added. The liquid phase of PGBCs was the same as that of PBC (MMA liquid). During the manipulation, the solid and liquid phases were mixed at a ratio of 2.0 g:1 mL.

C: **P(MMA-AA-St) mixed with GO bone cement** (**PGBCm**, in which m means mixing): P(MMA-AA-St)\GO powder was obtained by mixing 0.5 wt% GO into P(MMA-AA-St) and ball milling the mixture for 24 h. The solid phase of PGBCm was obtained by mixing and ball milling the P(MMA-AA-St)\GO powder and commercial PBC powder (Mendec® Spine 1230) at a volume ratio of 1:1. The X-ray contrast agent of PGBCm was also originated from PBC powder and no additional $BaSO_4$ was added. The liquid phase was the same as that of PBC. The solid and liquid phases were manipulated at a ratio of 2.0 g:1 mL.

The detailed composition of PBC, PGBCs, and PGBCm was listed in Table S1.

2.2. Material characterization

2.2.1. Raman spectroscopy

The GO-related chemical composition of P(MMA-AA-St)-GO was identified using a LabRAM HR Evolution spectrometer (Horiba Scientific, Longjumeau, France). Samples were excited with a 532-nm laser with an accumulating time of 30 s.

2.2.2. Transmission electron microscopy (TEM)

TEM was performed with a Tecnai G2 F20 system (FEI Co., Hillsboro, OR, USA) at an accelerating voltage of 200 kV. P(MMA-AA-St)-GO particles and GO nanosheets were ultrasonically dispersed in anhydrous ethanol respectively. The sample suspension was then dripped on a 200-mesh copper grid and dried, and then the morphology and microstructure of GO and P(MMA-AA-St)-GO were detected and imaged by TEM.

2.2.3. Scanning electronic microscopy (SEM)

Particles of PMMA, P(MMA-AA-St), and P(MMA-AA-St)-GO were dispersed in anhydrous ethanol with the assistance of ultrasound to form sample suspensions. Then, a sample of each suspension was dripped onto a silicon chip 10 mm × 10 mm in size and air-dried at room temperature using the ethanol evaporation procedure. Subsequently, the samples were platinum-sputtered, observed, and imaged by SEM (Hitachi S-4800, Japan).

2.2.4. Porosity evaluation

The porosity of PBC, PGBCs, and PGBCm was analysed using micro-CT scanning. The samples were prepared by mixing the cement at a ratio of 1 g: 0.5 mL at room temperature followed by water absorption in phosphate-buffered saline (PBS, Corning, NY, USA). Thereafter, the samples were dried and scanned using a micro-CT imaging system (AX2000, Always Imaging, China) at a solution of 3.8 μm, 90Kv, and 70 μA. The obtained CT data were reconstructed and analysed using the software VGstudio MAX 3.0.2 (Volume Graphics, Heidelberg, Germany). A cylindrical volume of interest (VOI) with 6 mm in height and 4 mm in diameter was selected to quantitatively analyze the porosity and the pore size.

2.2.5. Mechanical testing

The compressive strength test was performed according to ISO 5833:2002 to evaluate the biomechanics of PBC, PGBCs, and PGBCm before and after immersion in PBS. The surfaces of cylindrical samples (Φ6 × 12 mm) were ground using 3000-mesh sandpaper to ensure that the superior and inferior surfaces were parallel to each other. Thereafter, the samples were compressed using a universal material testing machine (Chuan Bei WDW-20, Jinan, China) at a loading speed of 20 mm/min; the loading ceased when the cylinder fractured or the upper yield point was reached. The change in loading force and displacement was automatically recorded and converted to the corresponding stress–strain curve. The compressive strength (MPa) was determined as the loading force divided by the cross-sectional area of the specimen, and the corresponding slope of the linear part of the stress–strain curve was taken as the elastic modulus. Five samples from each group were measured.

2.2.6. Curing test

The curing parameters, including the dough time (t_{dough}, n = 5), setting time (t_{set}, n = 3), setting temperature (T_{set}, n = 3) and maximum temperature (T_{max}, n = 3), were determined according to the standard of *Implants for surgery — Acrylic resin cements* (ISO5833:2002).

2.2.7. Water uptake

The water absorption rate and volume expansion rate of PBC, PGBCs, and PGBCm were tested as described in a previous study using the formulas listed below. Briefly, the sample was placed in PBS immediately after being mixed at the predetermined solid/liquid ratio for 1 h to allow for full water absorption. The mass was then weighed after the water on the surface of the sample was removed. The bulk of the tested sample after water absorption was examined by the *Archimedes* principle. The water absorption and volume expansion were calculated, and five samples from each group were tested.

$$WA = [(Ma - Mi)/Mi] \times 100\% \quad (1)$$

in which WA is the water absorption, Mi is the initial mass, and Ma is the mass after water absorption.

$$VE = [(Va - Vi)/Vi] \times 100\% \quad (2)$$

in which VE is the volume expansion, Vi is the initial volume, and Va is the volume after water absorption.

2.3. In vitro cell biocompatibility

2.3.1. Primary osteoblast isolation and characterization

2.3.1.1. Isolation of primary osteoblasts. The animal experiments in this study were conducted under the Guidelines for the Care and Use of Laboratory Animals and approved by the Laboratory Animal Welfare and Ethics Committee of Air Force Medical University.

Primary osteoblasts were isolated from 2-day-old neonatal Sprague−Dawley (SD) rats (Laboratory Animal Center of Air Force Medical University, Xi'an, China) according to a previously reported method [49].

After the SD rat was sacrificed by cervical dislocation and sterilized with 75% alcohol, the calvaria were excised, washed, and scraped thoroughly to remove attached soft tissue until the calvaria appeared semi-transparent. Thereafter, the calvaria were cut into fragments 1.0 mm × 1.0 mm in size and incubated in 0.25% trypsin-EDTA (Gibco, CA, USA) for 15 min at 37 °C. Then, the fragments were seeded in a 25-cm^2 flask and cultured with alpha minimum essential medium (α-MEM, Corning, NY, USA) containing 10% foetal bovine serum (FBS, Gibco, CA, USA), 100 U/ml penicillin and 100 μg/mL streptomycin (HyClone, CA, USA) in a humidified atmosphere of 5% CO_2 at 37 °C. The medium was changed every two days. Primary osteoblasts were harvested by trypsinizing the adherent cells that migrated from the calvaria and subcultured. Cells at passages 2–4 were used in subsequent experiments.

2.3.1.2. Primary osteoblast characterization. Primary osteoblasts were characterized by alkaline phosphatase (ALP) and Alizarin red S (ARS) staining. The harvested cells were seeded in a 6-well plate at a density of 5×10^5/mL. ALP staining was performed after the cells were cultured for 1 week using a BCIP/NBT Alkaline Phosphatase Colour Development Kit (Beyotime, Shanghai, China) according to the manufacturer's instructions. ARS staining was performed after the cells were cultured for 4 weeks using an ARS Staining Kit for Osteogenesis (Beyotime, Shanghai, China) to detect the mineralization of primary osteoblasts according to the manufacturer's instructions.

2.3.2. Cell proliferation

Cement extracts were prepared to evaluate the effects of PBC, PGBCs and PGBCm on cell proliferation according to the protocol of ISO 10993 and the reported literature [23,35,50]. The samples of PBC, PGBCs and PGBCm were prepared as ball shapes and irradiated by ^{60}Co at a dose of 25 kGy for sterilization. Thereafter, samples from each group were placed into disposable sterile tubes, sealed with caps, and incubated in α-MEM (0.2 g/mL) at 37 °C for 48 h to obtain cement extracts. The cement extracts were then supplemented with 10% FBS, 100 U/mL penicillin and 100 μg/mL streptomycin for cell culture.

2.3.2.1. CCK-8 assay. Primary osteoblasts were seeded in a 96-well plate at a density of 1×10^4/mL (1×10^3/well) and incubated at 37 °C/5% CO_2 for 24 h. Then, the medium was replaced with 100 μL of bone cement extract or full α-MEM (as a control) and changed every 2 days. After 1, 4, and 7 days of culture with the cement extracts, a Cell Counting Kit-8 assay (CCK-8, APExBIO, Hu, USA) was conducted according to the manufacturer's instructions. Cell viability was determined as the absorbance measured at 450 nm using a microplate reader (BioTek, VT, USA).

2.3.2.2. Live/dead cell staining. Primary osteoblasts were seeded in a 24-well plate (1×10^4 cells/well) and incubated at 37 °C/5% CO_2 for 24 h. The medium was replaced with 1 mL of cement extract or full α-MEM (as a control). On day 4, live/dead cell staining was carried out using a LIVE/DEAD™ Cell Imaging Kit (Invitrogen, CA, USA). Briefly, the staining solution was prepared by mixing live-green and dead-red solutions at a ratio of 1 mL:1 μL. The cells were washed with PBS three times, and then 0.2 mL of staining solution was added to each well. The cells were then incubated for 15 min at ambient temperature. Finally, the cells were washed twice with PBS and imaged by fluorescence microscopy (Zeiss, Heidenheim, Germany). The cell viability quantification of Live/dead cell staining was performed using Image J software (Wayne Rasband, NIH, USA).

2.3.2.3. Flow cytometry. The apoptosis of osteoblasts cultured with the cement extracts was determined using flow cytometry. Cells were seeded in a 6-well plate at a density of 1×10^6/mL and treated with cement extracts or full α-MEM (as a control). On days 4 and 7, the cells in each group were trypsinized and collected by centrifugation at 1000 rpm for 5 min. Then, the collected cells were rinsed with PBS and recentrifuged twice. Flow cytometry was performed using an Annexin V-FITC/PI Apoptosis Detection Kit (Yeasen, Shanghai, China). Briefly, the cell pellet was resuspended in 100 μL of binding buffer and then incubated with Annexin V-FITC and PI staining solution in the dark for 15 min. After adding 400 μL of binding buffer, the samples were analysed by an Epics XL-MCL flow cytometer (Beckman Coulter, CA, USA).

2.3.3. Cell attachment

Primary osteoblasts were seeded on sample discs (φ1.4 cm and ^{60}Co irradiated) and placed in a 24-well plate at a density of 1×10^4 cells/well. On days 4 and 7, the discs seeded with osteoblasts were washed three times with PBS and fixed with 2.5% glutaraldehyde. Then, the sample discs were dehydrated by a gradient series of ethanol concentrations up to 100%. Subsequently, the sample discs were completely vacuum-dried and sputter-coated with gold. The morphology of the cells seeded on the sample discs was observed and imaged by SEM (Hitachi, S–3000 N, Japan) at 5.0 kV.

2.3.4. Quantitative real-time polymerase chain reaction (qRT–PCR)

The bottom of a 6-well plate was coated with PBC, PGBCs, and PGBCm at a thickness of approximately 1 mm and irradiated by ^{60}Co before cell seeding. Coated and noncoated (as a control) 6-well plates were seeded with primary osteoblasts at a density of 1×10^6 cells/well. On day 7, the cells were washed three times with cold PBS, total RNA was collected using TRIzol Reagent (Invitrogen, CA, USA), and cDNA was synthesized using the First Strand cDNA Synthesis Kit (Servicebio, Wuhan, China) according to the manufacturer's instructions. Thereafter, qRT–PCR was performed in triplicate using the housekeeping gene β-actin as an endogenous control to determine the relative transcript levels of the osteogenic marker genes *Alp*, osteopontin (*Opn*), and Smad family member 5 (*Smad5*) using qPCR Master Mix according to the manufacturer's protocol (Servicebio, Wuhan, China). The primer sequences were designed and validated using the online tool Primer-BLAST and synthesized by Sangon Biotech (Sangon, Shanghai, China) (Table 1). The qRT–PCR data were analysed using the ΔΔCt method.

2.3.5. Western blotting

The cell culture procedure was the same as that reported in Section 2.3.4. On day 7, the cells were washed three times with cold PBS. Protein extraction was performed by adding 500 μL of RIPA supplemented with protease inhibitor (Thermo Scientific, CA, USA) to each well for cell lysis. Then, the cell lysate was centrifuged to collect the supernatant. The protein concentration was determined using the Pierce BCA Protein Assay Kit (Thermo Scientific, CA, USA). Sodium dodecyl sulphate–polyacrylamide gel electrophoresis (SDS–PAGE) was performed to separate proteins, and the separated proteins were transferred onto a polyvinylidene fluoride (PVDF) membrane. Thereafter, the PVDF membrane was blocked in Tris-buffered saline with Tween (TBST) containing 5% nonfat milk for 1 h, thoroughly blocked with TBST three times, transferred to the primary antibody solution and incubated at 4 °C overnight. The TBST washing procedure was repeated, and then the PVDF membrane was incubated in the tagged secondary antibody solution for 1 h at room temperature. The PVDF membrane was rinsed three times with TBST, prepared using Pierce™ ECL Western blotting Substrate (Thermo Scientific, CA, USA), and detected under a chemiluminescence imaging system (Tanon, Shanghai, China).

The primary antibodies were β-actin antibody (Abcam, Cambridge, UK), OPN antibody (Abcam, Cambridge, UK), and Smad5 antibody (GeneTex, CA, USA). The secondary antibody was horseradish peroxidase-tagged anti-rabbit IgG antibody (KPL SeraCare, MA, USA). Both the primary antibody and secondary antibody were diluted at a ratio of 1:1000.

Table 1
The primer sequence of qRT-PCR.

Gene	Sequence		Prod Size (bp)	Tm (°C)	Access ID
ALP	F	CCTTAGGGCCACCGCTCG	74	62.53	NM_013059.2
	R	GTTAATTGACGTTCCGATCCTGC		60.24	
OPN	F	CCAGCCAAGGACCAACTACA	132	59.60	NM_012881.2
	R	AGTGTTTGCTGTAATGCGCC		59.76	
Smad-5	F	GCCGTTTGCAAGTCTCTCAC	198	59.76	NM_021692.1
	R	ACACTGGAGGTAAGACTGGAC		58.75	
β-actin	F	CCCGCGAGTACAACCTTCTTG	71	61.27	NM_031144.3
	R	GTCATCCATGGCGAACTGGTG		61.61	

F and R mean forward primer and reward primer, respectively.

2.4. In vivo biocompatibility evaluation

2.4.1. Rabbit surgery

Eighteen New Zealand rabbits (Laboratory Animal Center of Air Force Military University, Xi'an, China) were randomized into three groups to evaluate the *in vivo* biocompatibility of the materials. All rabbits were acclimated to the new cultivation environment and fed a standard diet for one week before surgery. Rabbits were anaesthetized by the intermuscular administration of xylazine hydrochloride (0.2 mL/kg) and 2% pentobarbital sodium (0.4 mL/kg). The hair of the left hindlimb was shaved carefully after the rabbit was well anaesthetized. The rabbit was then placed on and fixed to the operating table. The surgical site was disinfected with povidone-iodine and routinely prepared for aseptic surgery. A mid-lateral longitudinal incision was made on the lower thigh and extended to the knee joint. All perijoint ligaments and articular capsules were well protected. Then, subcutaneous and muscular mantle dissection and muscle retraction were performed to expose the periosteum. After the lateral side of the femoral condyle was prepared, a bone defect (approximately 10.0 mm in depth and 4.0 mm in diameter) was made using a drill and then filled with prepared materials mixed at a powder/liquid ratio of 2 g/mL. The surgical wound was closed layer-by-layer after verification that no active bleeding was occurring. One dose of penicillin (50000 U/kg) was given intramuscularly to prevent surgery-related infection. After recovering consciousness, the rabbits were returned to their cages and given a standard diet as before. The rabbits received daily care for their surgical wounds and general condition.

2.4.2. Radiological evaluation

One week postoperatively, when the status of the rabbits was stable, an X-ray examination (DRX-1, Carestream Health, USA) was performed to check the location of the bone cement and the condition of the surrounding soft tissues. After the rabbit was fully anaesthetized as described above, lateral and anterior-posterior X-ray films were obtained for further evaluation.

2.4.3. Haematological testing

Blood samples were collected before and 1, 2, 3, and 4 weeks after surgery, and haematological and biochemical tests were performed to further assess the toxicity of the bone cement. Haematological parameters, including the white blood cell (WBC) count, red blood cell (RBC) count, haemoglobin (HGB), haematocrit (HCT), mean corpuscular volume (MCV), and platelet distribution width (PDW), were analysed with an autohaematology analyser (Mindray BC-2800 Vet, Shenzhen, China). Biochemical parameters, including total protein (TP), albumin (ALB), and blood urea nitrogen (BUN), were tested using an autobiochemistry analyser (Rayto Chemray 800, Shenzhen, China) with a reagent kit for each parameter. Then, the parameters were compared among groups at each time point.

2.4.4. Micro-CT scanning

The left femoral condyle was harvested from rabbits euthanized at 4 and 16 weeks after implantation, and the femur was prepared using a bone saw (Ameritool, CA, USA) to retain the femoral condyle for micro-CT scanning, which was performed using a FeinFocus X-ray system (YXLON, Hamburg, Germany) at 90 kV and 50 μA. Thereafter, the obtained CT data were processed using VGstudio MAX 3.0.2 (Volume Graphics, Heidelberg, Germany). After the femoral condyle was reconstructed, the microarchitecture of the bone region of interest (ROI, 200 μm around the implanted materials) was compared among the three groups using parameters including the bone volume fraction (BV/TV), trabecular number (Tb.N), and trabecular separation (Tb.Sp).

2.4.5. Histological evaluation

At 4 and 16 weeks after surgery, the left femoral condyle and the muscle adjacent to the bone cement implantation site were harvested to evaluate the local biocompatibility of the bone cement. The lungs, heart, liver, and kidneys of the rabbits were harvested to evaluate the whole-body biocompatibility of the bone cement. All harvested specimens were fixed in 4% paraformaldehyde until the staining procedure.

2.4.5.1. Haematoxylin & eosin (HE) staining and Masson trichrome staining. At 4 weeks after surgery, the femoral condyle was harvested and prepared as described above and decalcified using 15% EDTA solution, which was changed every 3 days. The endpoint of decalcification was determined by X-ray examination. After decalcification was achieved, the femoral condyle was exposed by an incision along the coronal plane of the cylindrical sample. Thereafter, the bone cement was gently removed while the bone tissues around the cement were collected. Samples were washed with tap water for 24 h, dehydrated with a gradient series of alcohol concentrations, clarified with xylene, and embedded in paraffin. Thereafter, the embedded specimen was cut into 5-μm sections, which were mounted onto glass slides, deparaffinized, and rehydrated for standard HE and Masson trichrome staining.

2.4.5.2. Van Gieson (VG) staining. At 16 weeks after surgery, the fixed left femoral condyle was prepared by removing the attached soft tissues and trimmed using a bone saw to dimensions suitable for placement into a glass embedding vial. The prepared femoral condyle was washed with tap water for 24 h, dehydrated, and clarified using an automatic tissue hydroextractor (KH-TK, Hubei, China). Then, the femoral condyle was placed in a glass embedding vial with the cutting surface face down and covered in self-hardening liquid resin (MMA 800 mL, dibutyl phthalate 200 mL, benzoyl peroxide 70 g). The vial was vacuum-evacuated at 4 °C for 8 h and then transferred to a 45 °C water bath overnight for resin curing. Bone sections with a thickness of 200 μm were obtained using a diamond saw (Leica SP 1600, Nussloch, Germany), placed on acrylic slides, ground to 50 μm using 2000-mesh sandpaper, and gently polished. All sections were then subjected to VG staining to evaluate and compare the bone-material interface between groups.

2.4.5.3. HE staining of adjacent muscle and vital organs. The muscle, lungs, heart, liver, and kidneys were harvested at 4 and 16 weeks after surgery and routinely fixed. Thereafter, samples were subjected to the same standard HE staining procedure, similar to the staining of decalcified femoral condyle samples mentioned above.

2.5. Statistical analysis

Descriptive data are expressed as the mean and standard deviation (M ± SD). Statistical analysis was performed using GraphPad Prism (version 8.3.1, CA, USA). One-way ANOVA followed by a multiple comparisons test was performed to detect differences between groups, and $P < 0.05$ was considered statistically significant.

3. Results

3.1. Synthesis of P(MMA-AA-St) and P(MMA-AA-St)-GO

The reaction solution before and after P(MMA-AA-St)-GO synthesis were shown in Fig. S1. The 0.5% GO nanosheet was evenly dispersed after continuously ultrasonicated and a dark reaction solution was obtained without apparent stratification or phase separation (Fig. S1A). While after polymerization and the crude product of P(MMA-AA-St)-GO isolation, a clear and transparent solution was obtained (Fig. S1B). This change of the reaction solution indicated that GO has fully synthesized with P(MMA-AA-St).

3.1.1. Raman spectroscopy

The obtained P(MMA-AA-St)-GO (Fig. S2) was characterized with Raman spectroscopy. Two characterized intensive bands, D and G, corresponding to the sp^3 hybridization of carbon atoms from the functional groups and in-plane sp^2 hybridization of carbon atoms, respectively, emerged at 1352 cm^{-1} and 1596 cm^{-1} in the GO Raman spectra, as shown in Fig. 1A [51]. When comparing the Raman spectra of GO and

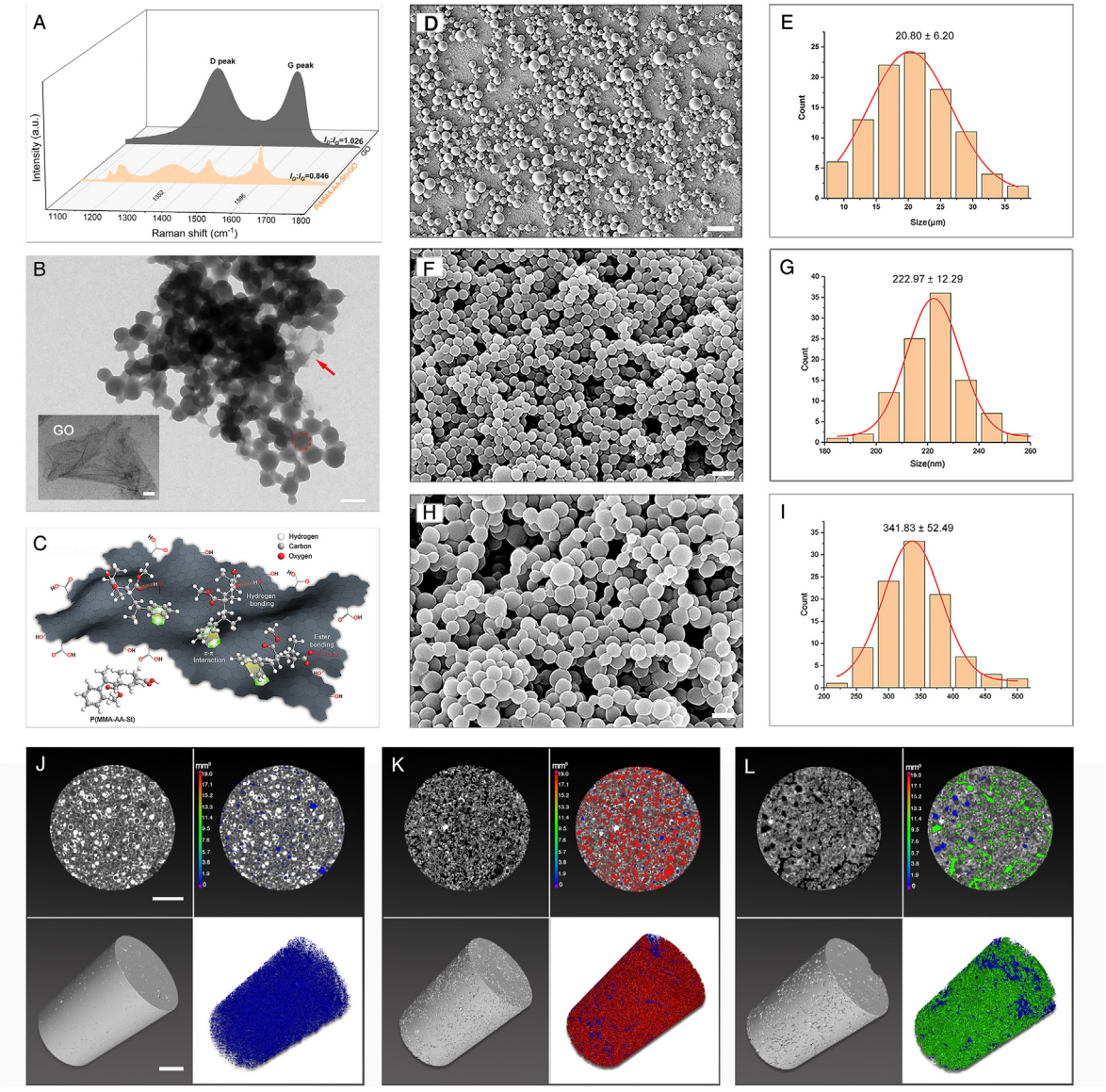

Fig. 1. Synthesis and characterization of P(MMA-AA-St) and P(MMA-AA-St)-GO. Raman spectra (A) of GO and P(MMA-AA-St)-GO. TEM images show that P(MMA-AA-St) (red dash circle) could be synthesized within the GO sheet to form P(MMA-AA-St)-GO (B) with the GO sheets (red arrow) wrapped around the P(MMA-AA-St) particles; the micrograph of GO sheet also illustrated in the lower left of Fig. 1B. Schematic of the chemical interaction between the GO sheet and P(MMA-AA-St) indicating π-π interactions between St and GO, hydrogen bonds between MMA and GO and between AA and GO, and ester bonds between AA and GO (C). Morphology of PMMA (D), P(MMA-AA-St) (F), and P(MMA-AA-St)-GO (H) and the corresponding spherical size distributions (E, G, I).The pores distribution of PBC (J), PGBCs (K), and PGBCm (L): the representative horizontal section (up-left) and 3D reconstruction of VOI (down-left), and the horizontal section view (up-right) and 3D reconstruction (down-right) of pores in the VOI (n = 4). (The scale bar is 500 nm for the GO sheet and 20 nm for B. The scale bar is 100 μm for D, and 400 nm for F and H. The scale bar is 1 mm for J-L and the colour scale bar in J-L indicated the volume of pores in PBC, PGBCs and PGBCm). (For interpretation of the references to color in this figure legend, the reader is referred to the Web version of this article.)

P(MMA-AA-St)-GO, the similar typical D peak and G peak appeared in the Raman spectra of P(MMA-AA-St)-GO indicated that GO was present in the P(MMA-AA-St)-GO nanocomposite. The intensity ratio of the characteristic D and G bands (I_D/I_G) was applied to evaluate the polymerization of P(MMA-AA-St)-GO (Table 2). The I_D/I_G of P(MMA-AA-St)-GO (0.846) was decreased when compared to that of pristine GO (1.026) which indicated a partial reduction of GO during the synthesis of P(MMA-AA-St)-GO. These characteristic features of the emergence of the D and G peaks and change in I_D/I_G indicated that GO was present in the P(MMA-AA-St)-GO nanocomposite.

3.1.2. Morphology observation

The morphology of the GO sheet and P(MMA-AA-St)-GO was also observed by TEM. The TEM micrographs of GO (Fig. 1B) revealed that the GO nanosheet was a thin flake with few wrinkles and folds [42,44]. The micrographs of P(MMA-AA-St)-GO (Fig. 1B) illustrated that P(MMA-AA-St) particles (red dash circle) were well wrapped by GO sheets.

The morphology of commercial PMMA particles and the synthesized P(MMA-AA-St) and P(MMA-AA-St)-GO particles was observed using SEM. PMMA (Fig. 1 D, E), P(MMA-AA-St) (Fig. 1F, G), and P(MMA-AA-St)-GO (Fig. 1H and I) particles all exhibited a regular spherical shape with a mean diameter of 20.80 ± 6.20 μm, 222.97 ± 12.29 nm and 341.83 ± 52.49 nm, respectively. Gaussian fitting (red line) revealed that the diameter of each sample was normally distributed.

3.1.3. Porosity and pore size

The reconstructed 3D and horizontal morphology of pores in PBC, PGBCs, and PGBCm (Fig. 1J, K, L) demonstrated significantly higher porosity of PGBCs and PGBCm than PBC. The porosity of PBC was 3.00 ± 0.74% which was in accordance with the reported porosity of the commercial Mendec Spine [52]. The porosity of PGBCs and PGBCm was significantly higher than that of PBC (22.83 ± 2.04% and 13.66 ± 1.56%, both $P < 0.0001$, respectively). In addition, the porosity of PGBCs was also significantly higher than PGBCm ($P < 0.0001$). The diameter of the pores detected in the samples of PBC, PGBCs, and PGBCm were 33.32 ± 0.95 μm, 50.50 ± 6.53 μm, and 60.29 ± 10.23 μm, respectively. The diameters of the pores in PGBCs and PGBCm were larger than that in PBC ($P = 0.0178$ and $P = 0.0011$).

3.2. Characterization of properties

3.2.1. Water uptake and volumetric expansion

Both PGBCs and PGBCm have a high capacity for water uptake. The water absorption ratio of PGBCs and PGBCm was 95.14 ± 5.71% and 78.10 ± 2.60%, respectively, while that of PBC was −0.04 ± 0.06% (Fig. 2A). The volume of PBC after immersion in PBS shrank by approximately −5.07 ± 0.37%, while that of PGBCs and PGBCm expanded by approximately 101.18 ± 5.31% and 83.36 ± 3.49%, respectively (Fig. 2B) under the same conditions.

3.2.2. Mechanical properties

Representative stress–strain curves of PBC, PGBCs, and PGBCm are illustrated in Fig. 2C. The compressive strength of PGBCs and PGBCm (99.20 ± 1.64 MPa and 74.0 ± 4.64 MPa, respectively) was slightly less than that of PBC (109.20 ± 0.84 MPa) (Fig. 2D). After immersion in PBS, the compressive strength of PGBCs and PGBCm was 75.60 ± 3.05 MPa and 60.20 ± 2.77 MPa, respectively, while that of PBC was not significantly changed (103.20 ± 5.54 MPa) (Fig. 2E). The elastic modulus of PGBCs and PGBCm (2596.26 ± 55.93 MPa and 1772.19 ± 219.27 MPa, respectively) was significantly lower than that of PBC (2911.77 ± 215.17 MPa, $P = 0.0420$ and $P < 0.0001$, respectively) (Fig. 2F). Meanwhile, the elastic modulus of PGBCs and PGBCm detected after immersion in PBS was significantly lower than that of the immersed PBC (Fig. 2G).

Table 2
Summary of the D/G ratio determined from the Raman spectroscopy.

Sample	D band	G band	I_D:I_G ratio
GO	6557.48	6391.93	1.026
P(MMA-AA-St)-GO	1585.76	1874.19	0.846

3.2.3. Curing properties

Representative time–temperature curves of each bone cement are shown in Fig. 2H. The T_{set} of PGBCs and PGBCm was significantly lower than that of PBC (58.57 ± 1.83 °C and 60.82 ± 2.45 °C *vs.* 69.35 ± 1.26 °C, $P = 0.0011$ and $P = 0.0038$, respectively) (Fig. 2I). The T_{max} of the first two was also lower than that of PBC (94.67 ± 3.77 °C and 98.60 ± 4.62 °C *vs.* 115.23 ± 2.41 °C, $P = 0.0012$ and $P = 0.0037$, respectively) (Fig. 2J). The t_{dough} of PGBCs and PGBCm was longer than that of PBC (7.00 ± 0.22 min and 6.95 ± 0.37 min *vs.* 4.30 ± 0.25 min, both $P < 0.0001$) (Fig. 2K), and the t_{set} of PGBCs was longer than that of PBC (10.76 ± 1.92 min *vs.* 6.53 ± 0.42 min, $P = 0.0381$), while no significance was detected between that of PGBCm (8.59 ± 1.89 min) and that of PBC (Fig. 2L).

3.3. In vitro biocompatibility

3.3.1. Primary osteoblast isolation and characterization

Primary osteoblasts emerged from the digested calvarial bone fragments after being cultured in full α-MEM for one day and gradually proliferated around the bone fragments (Fig. 3A–F). The primary osteoblasts were characterized by ALP staining and ARS staining. ALP staining revealed the formation of typical purple deposits in the cytoplasm, which represented intracellular ALP (Fig. 3G and H) [53,54]. After the isolated primary osteoblasts (4th generation) were cultured for four weeks, mineralized calcium nodes could be detected by microscopy (Fig. 3I and J). ARS staining also revealed the mineralization of calcium nodes, which exhibited typical red deposits (Fig. 3K and L) [55,56].

3.3.2. Cell compatibility

The CCK-8 assay revealed that the cell viability of PGBCs and PGBCm was significantly higher than that of PBC after osteoblasts were cultured with the cement extracts for 1, 4, and 7 days. However, the viability of osteoblasts in the PGBCm group was still lower than that in the control group. But no significant difference in osteoblast viability was detected between the PGBCs and the control group (Fig. 4A). The results of live/dead cell staining were consistent with those of the CCK-8 assay. More dead cells were detected after the osteoblasts were cultured with the PBC extract than with the PGBCs and PGBCm extracts (Fig. 4B). The quantification of live/dead cell staining indicated that the cell viability of PBC group and PGBCm group was significantly lower than that of control group ($P < 0.0001$, $P = 0.008$), while no statistical significance was detected between the cell viability of PGBCs group and that of control group ($P = 0.2003$). Besides, the cell viability of PGBCs group and PGBCm group was significantly higher than that of PBC group (both $P < 0.0001$) (Fig. 4D). Flow cytometry analysis revealed that the 4-day apoptosis rate of the osteoblasts cultured with the PBC, PGBCs and PGBCm extracts was 2.77 ± 0.39%, 2.40 ± 0.53% and 2.37 ± 0.38%, respectively, while the 7-day apoptosis rate was 4.43 ± 0.55%, 3.67 ± 0.59%, and 4.00 ± 0.66% (Fig. 4C). Both the 4-day and 7-day apoptosis rates of the osteoblasts cultured with PBC extract were significantly higher than those in the Control group ($P = 0.0370$, $P = 0.0066$). No significant difference was detected in the apoptosis rate of osteoblasts cultured with PGBCs or PGBCm extract when compared to the Control group, with the exception of the 7-day apoptosis rate of PGBCm ($P = 0.0246$). The results of the CCK-8 assay, live/dead cell staining, and apoptosis rate all indicated that the cytocompatibility of PGBCs was superior to that of PBC.

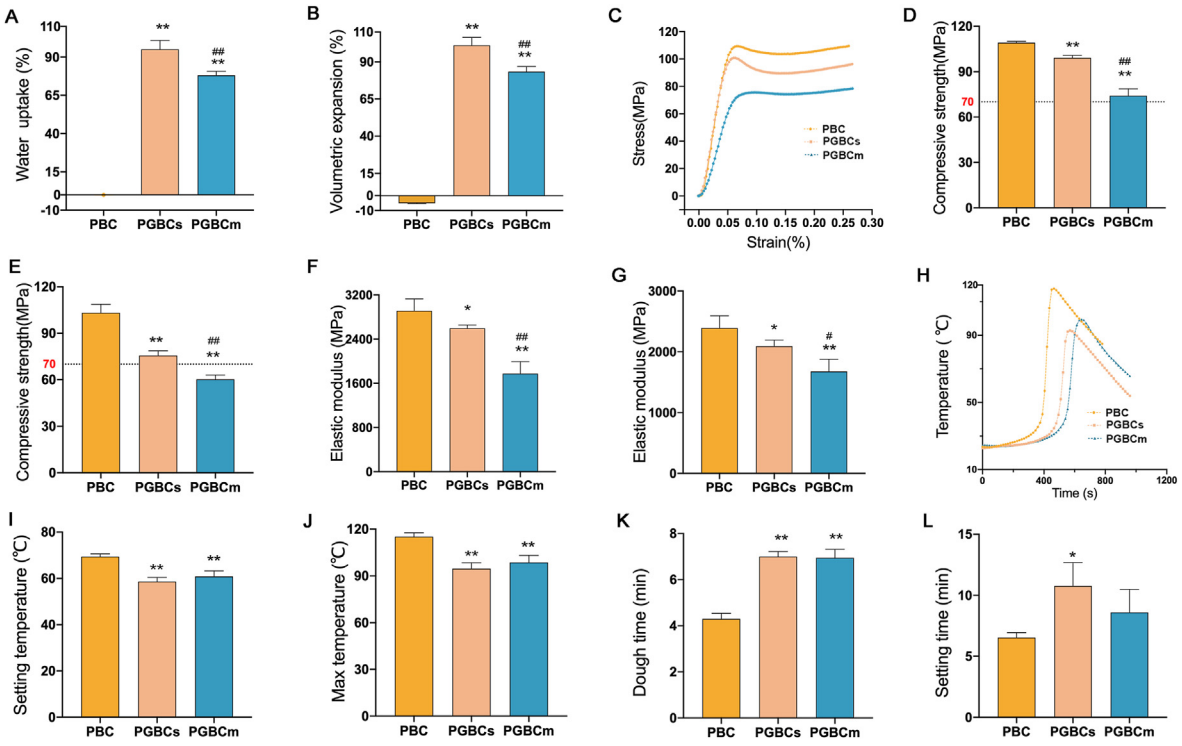

Fig. 2. Characterization of the properties of the bone-filling materials. Water uptake (A) and volumetric expansion (B) of PBC, PGBCs, and PGBCm(n = 5). Representative stress-strain curves (C), compressive strengths (D, E), and elastic moduli (F, G) of the materials before (D, F) and after (E, G) water immersion (n = 5). Representative time-temperature curves (H), setting temperatures (I, n = 3), max temperatures (J, n = 3), dough times (K, n = 5), and setting times (L, n = 3) of each bone cement. (* indicates a significant difference between PGBCs or PGBCm and PBC, *P < 0.05, **P < 0.005; # indicates a significant difference between PGBCs and PGBCm, #P < 0.05, ##P < 0.005).

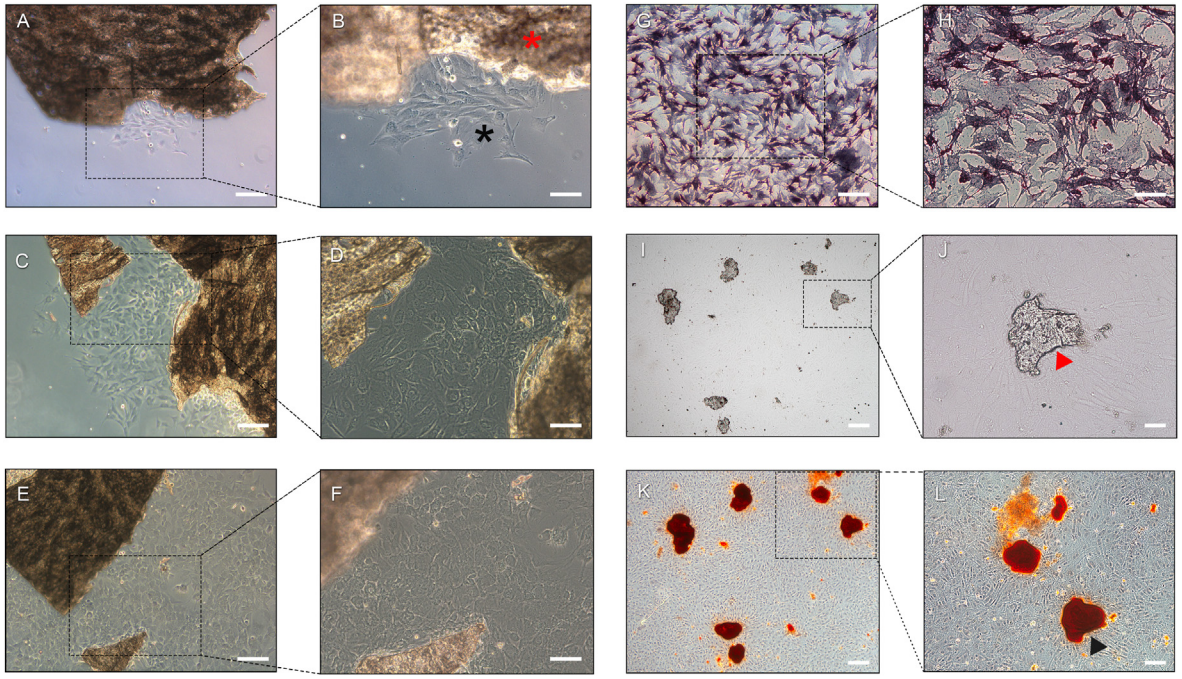

Fig. 3. Primary osteoblast isolation and characterization. After calvarial bone fragments were cultured in α-MEM for seven days, osteoblasts migrated from the edge of the bone fragments and proliferated around the fragments (A, B: 1 day; C, D: 4 days; E, F: 7 days; red star: bone fragment; black star: osteoblast). ALP staining indicated violet deposits in the cytoplasm representing intracellular ALP synthesized by primary osteoblasts (G, H). Optical micrograph (I, G) and image of ARS staining (K, L) of mineralized calcium nodules formed after isolated primary osteoblasts were cultured for four weeks (red triangle: unstained calcium nodule; black triangle: ARS-stained mineralized nodule). K and L are the stained versions of I and J, respectively. (The scale bar is 100 μm for A – I and K, 50 μm for J, 100 μm for L). (For interpretation of the references to color in this figure legend, the reader is referred to the Web version of this article.)

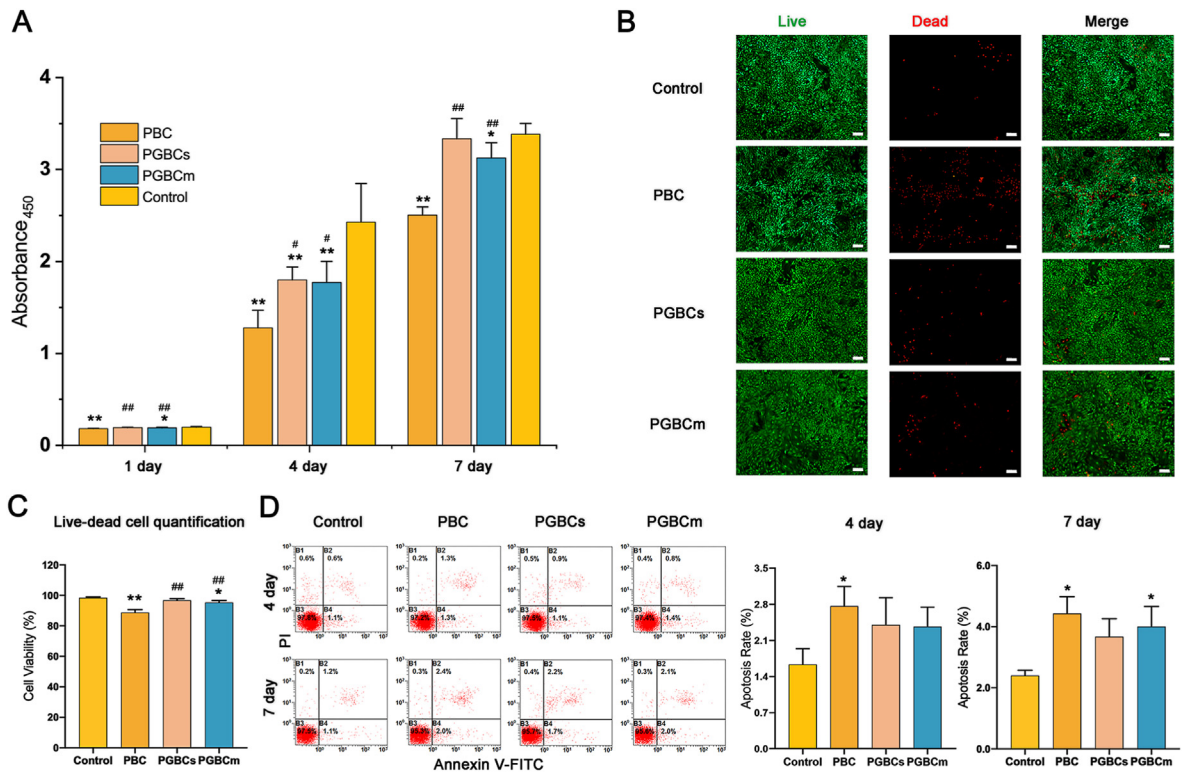

Fig. 4. Cytocompatibility of the materials. (A) The toxicity of the materials was evaluated using a CCK-8 assay after osteoblasts were cultured for 1, 4, and 7 days with material extracts. The results indicated greater osteoblast viability in the PGBCs group than in the PBC group (n = 8). (B) Live/dead cell staining (live: green; dead: red; scale bar, 200 μm) revealed more dead cells (red) in the PBC group than in the control group (n = 3). (C) The cell viability quantification of Live/dead cell staining (n = 3). (D) The 4- and 7-day apoptosis rates of osteoblasts cultured with extracts were tested using flow cytometry (n = 3). The results indicated the highest osteoblast apoptosis rate in the PBC group, with a statistically significant difference from the control group. (* and ** indicate $P < 0.05$ and $P < 0.001$ compared to the control group; # and ## indicate $P < 0.05$ and $P < 0.001$ compared to the PBC group. Data are presented as the mean ± standard deviation). (For interpretation of the references to color in this figure legend, the reader is referred to the Web version of this article.)

3.3.3. Cell attachment

The morphology of the osteoblasts was observed by SEM to detect the interaction between the osteoblasts and bone cement. Surface scanning of the material revealed that PGBCs and PGBCm had higher surface roughness than PBC, which was in accordance with our previous findings [35]. The 4-day and 7-day osteoblast attachment data are shown in Fig. 5A; osteoblasts showed less spreading on PBC than on PGBCs and PGBCm. In addition, osteoblasts were prone to elongation rather than an even distribution on the surface of PBC. Better osteoblast attachment was detected on the surface of PGBCs and PGBCm, with the cells exhibiting a larger spreading area.

3.3.4. Osteogenic expression

The osteogenic interference of PGBCs and PGBCm was detected and compared to that of PBC by RT–PCR and Western blot analysis. As shown in Fig. 5B, the expression levels of *Alp*, *Opn*, and *Smad5* in osteoblasts after 7 days of culture on PGBCs and PGBCm were significantly upregulated compared with those in osteoblasts cultured on PBC or osteoblasts cultured in the control group. In addition, the Western blot results were consistent with the levels of gene expression. The protein expression levels of OPN and Smad5 in the PGBCs and PGBCm groups were significantly higher than those in the control and PBC groups (Fig. 5C).

3.4. In vivo biocompatibility

3.4.1. General condition and X-ray observation

PBC, PGBCs, and PGBCm could all be implanted well into the femoral condyle defect (Fig. 6A–E); no cases of surgical-site infection occurred, and all wounds healed well after surgery. X-ray observation demonstrated that all three materials had satisfactory radiopaque properties and filled the bone defects well. This indicated that PGBCs and PGBCm retained suitable radiopacity which satisfied the clinical application despite the content of $BaSO_4$ being reduced by half due to the replacement of half the solid phase with P(MMA-AA-St)-GO or P(MMA-AA-St)\GO nanocomposite. In addition, no obvious inflammatory signs were detected in the bone around the materials or in the adjacent tissues (Fig. 6F–H).

3.4.2. Micro-CT scanning

Reconstruction of the femoral condyle was performed after micro-CT scanning to detect the microarchitecture of the bone around the implanted bone cement (Fig. 6). The 4-week BV/TV in the PGBCs group was significantly higher than that in the PBC group ($P = 0.009$) and PGBCm group ($P = 0.016$). The 16-week BV/TV in the PGBCs group was also significantly better than that in the PBC group ($P = 0.001$) and PGBCm group ($P = 0.045$). In addition, the 16-week BV/TV in the PGBCm group was significantly higher than that in PBC group ($P = 0.023$) (Fig. 6L). The 16-week Tb.N in PGBCs group was 1.82-fold higher than that in the PBC group ($P = 0.008$) (Fig. 6M). However, the 16-week Tb.Sp in the PBC group was 1.98-fold and 1.40-fold higher than that in PGBCs group ($P = 0.003$) and PGBCm group ($P = 0.031$), respectively (Fig. 6N).

3.4.3. Haematological and biochemical testing

Haematological testing indicated no significant differences among the PGBCs, PGBCm, and PBC groups in the WBC count, RBC count, HGB, HCT, MCV, or PDW, with the exception of the 3-week RBC count, which was significantly higher in PGBCs group than in the PBC group ($P = 0.0290$) (Fig. 7A). Moreover, biochemical testing performed at the same time point demonstrated no statistically significant differences in TP,

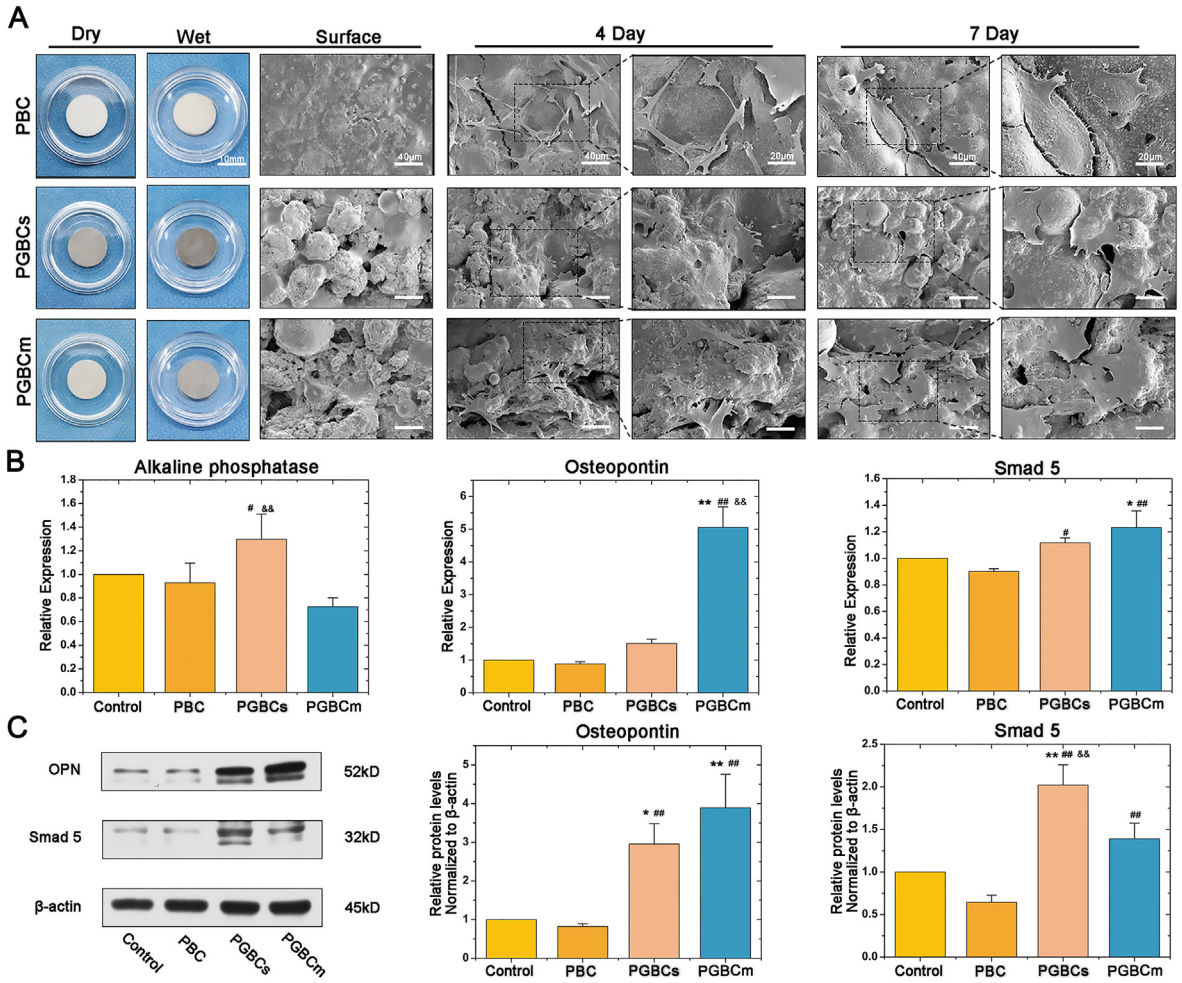

Fig. 5. Cell attachment, osteogenic gene, and protein expression of osteoblasts after being cultured with materials. Better osteoblast attachment was observed on the surface of PGBCs and PGBCm than on PBC (A). The RT–PCR results indicated that GO-modified PGBCs and PGBCm could improve osteogenic gene expression (B). Similar trends of osteogenic protein expression were detected by Western blotting, and the corresponding semiquantitative results of OPN and Smad5 expression were determined according to the intensity of the protein band (C). (n = 3 and the experiment triplicated, * and ** indicate $P < 0.05$ and $P < 0.005$ compared to the control group; # and ## indicate $P < 0.05$ and $P < 0.005$ compared to the PBC group; && indicates $P < 0.005$ when comparing PGBCs to PGBCm. Data are presented as the mean ± standard deviation. The diameter of the sample was ~14 mm identically and the scale bar is 10 mm for the samples. The scale bar is 40 μm for the Surface, the 1st column 4-day and 7-day SEM images. The scale bar is 20 μm for the 2nd column 4-day and 7-day SEM images).

ALB, or BUN among the groups, with the exception of the 3-week TP, which was significantly higher in the PBC group than in the PGBCm group ($P = 0.0482$) (Fig. 7B). Neither haematological nor biochemical testing indicated obvious blood toxicity after PBC, PGBCs, or PGBCm implantation.

3.4.4. HE, Masson, and VG staining of the femoral condyle

Representative images of HE-stained decalcified femur condyles harvested four weeks after surgery revealed a lower trabecular number and thickness and a large amount of fatty tissue in the trabecular interstices in the PBC group compared with the other two groups. In addition, the formation of effluent collagen matrix, which was stained blue by Masson trichrome staining (Fig. 8A), was observed in the PGBCs and PGBCm groups, while collagen synthesis was seldom detected in the PBC group. The images of VG-stained undecalcified femur condyles harvested at 16 weeks after surgery showed an obvious linear space between the bone and cement in the PBC group but not in the PGBCs or PGBCm group (Fig. 8B).

3.4.5. HE staining of adjacent muscle and vital organs

HE staining of the lungs, heart, liver, and kidneys performed at 4 weeks (Fig. 9) and 16 weeks (Fig. S4) after surgery revealed no remarkable morphological differences in vital organs among the groups. The HE staining of the muscle adjacent to the site of bone cement implantation revealed no obvious inflammatory cell infiltration, and the morphology of the muscle cells was normal and identical among the groups.

4. Discussion

Currently, PBC is a commonly used filling and grouting material in orthopaedic surgery. However, there are shortcomings, including volumetric shrinkage, high elastic modulus, toxicity, and poor osteointegration, that prevent PBC from being an ideal material. In our previous study, volumetric shrinkage was well addressed through water uptake-generated expansion, which was realized by introducing the hydrophilic substrate AA into PBC withsynthesized P(MMA-AA-St) [35]. However, the mechanical properties of the as-modified PBC did not meet the standards for bone cement despite the use of St to improve its mechanics. GO is a material with superior biomechanics and has been widely studied in the biomaterials field. It has been indicated to be an osteoblast-friendly material, with a favourable effect on osteogenesis when used to modify bone materials. According to the reported literature, the biomechanical reinforcement of PBC by GO is hindered when the doping percentage

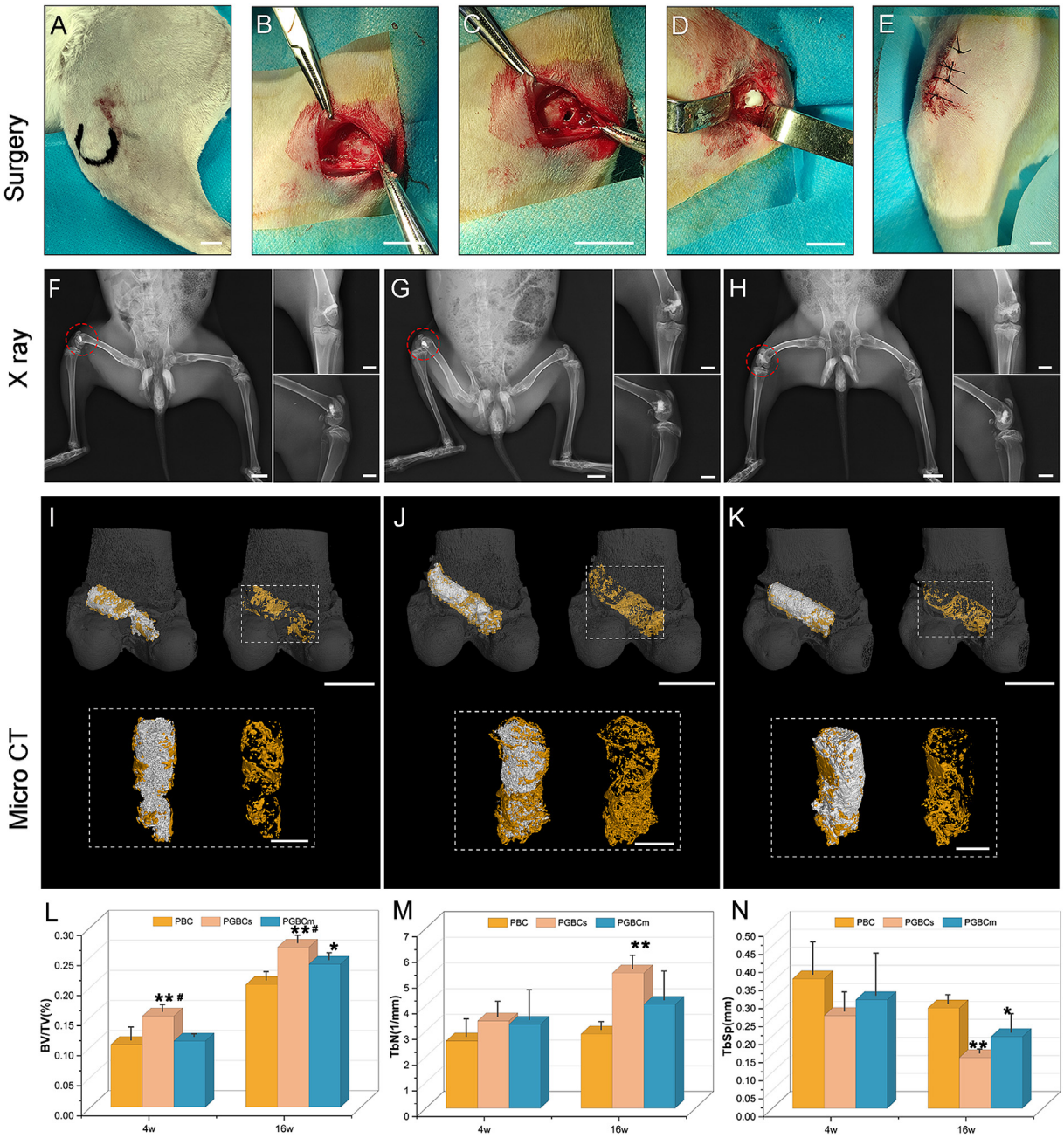

Fig. 6. Surgical procedure and radiological evaluation of materials implanted in rabbit femoral condyles. Femoral condyle location (A) and exposure (B), bone cavity drilling (C), bone cement injection (D), and wound closure (E) (6 rabbits in each group). Postoperative X-ray radiography performed after surgery indicated that PBC (F), PGBCs (G), and PGBCm (H) could fill the bone cavity well, and no inflammatory signs were detected. Bone regeneration surrounding PBC (I), PGBCs (J), and PGBCm (K) was analysed by micro-CT scanning at 4 and 16 weeks after surgery. The bone formation (pseudocolour yellow) in the ROI was compared using the microstructural parameters BV/TV (L), Tb.N (M) and Tb.Sp (N) (n = 3). PBC, PGBCs and PGBCm were reconstructed using the pseudocolour grey. (* and ** indicate $P < 0.05$ and $P < 0.01$ compared to the PBC group; # indicates $P < 0.05$ compared to the PGBCm group. Data are presented as the mean ± standard deviation. The scale bar is 1 cm for surgical image A-E. The scale bar is 2 cm for the lowest extremity and 1 cm for standard anterior-posterior and lateral X-ray radiography. The scale bar is 1 cm for the reconstructed femur condyle with implanted material and 5 mm for the reconstructed materials and surrounded bone tissues shown in dotted boxes in I, J, K). (For interpretation of the references to color in this figure legend, the reader is referred to the Web version of this article.)

exceeds 0.5 w/w% [43,44]. Furthermore, graphene-based materials play contrasting roles in the regulation of cell metabolism: the positive role is the facilitation of cell attachment and proliferation through the aforementioned mechanisms; the negative role is the simultaneous reduction in mitochondrial membrane potential and increase in intracellular reactive oxygen species (ROS) when used at high doses [57]. Elevated ROS levels can induce cell necrosis by damaging DNA. Therefore, 0.5 w/w% GO was chosen to reinforce P(MMA-AA-St) in this study according to previous literature and the results of the preliminary study.

The Raman spectra revealed the characteristic D and G bands that appeared in P(MMA-AA-St)-GO, indicating that GO was successfully incorporated into P(MMA-AA-St) (Fig. 1). The decreased I_D/I_G ratio in the case of P(MMA-AA-St)-GO was attributed to the proportion of sp^3 hybridized carbon atom in the GO restored to sp^2 conjugation, indicating a partial reduction of GO during synthesis, the same decreasing trend of I_D/I_G values detected in the previous literature about PS/GO compound [58–60]. This observation also demonstrated the successful participation of GO in the polymerization reaction. In addition, the π–π stacking

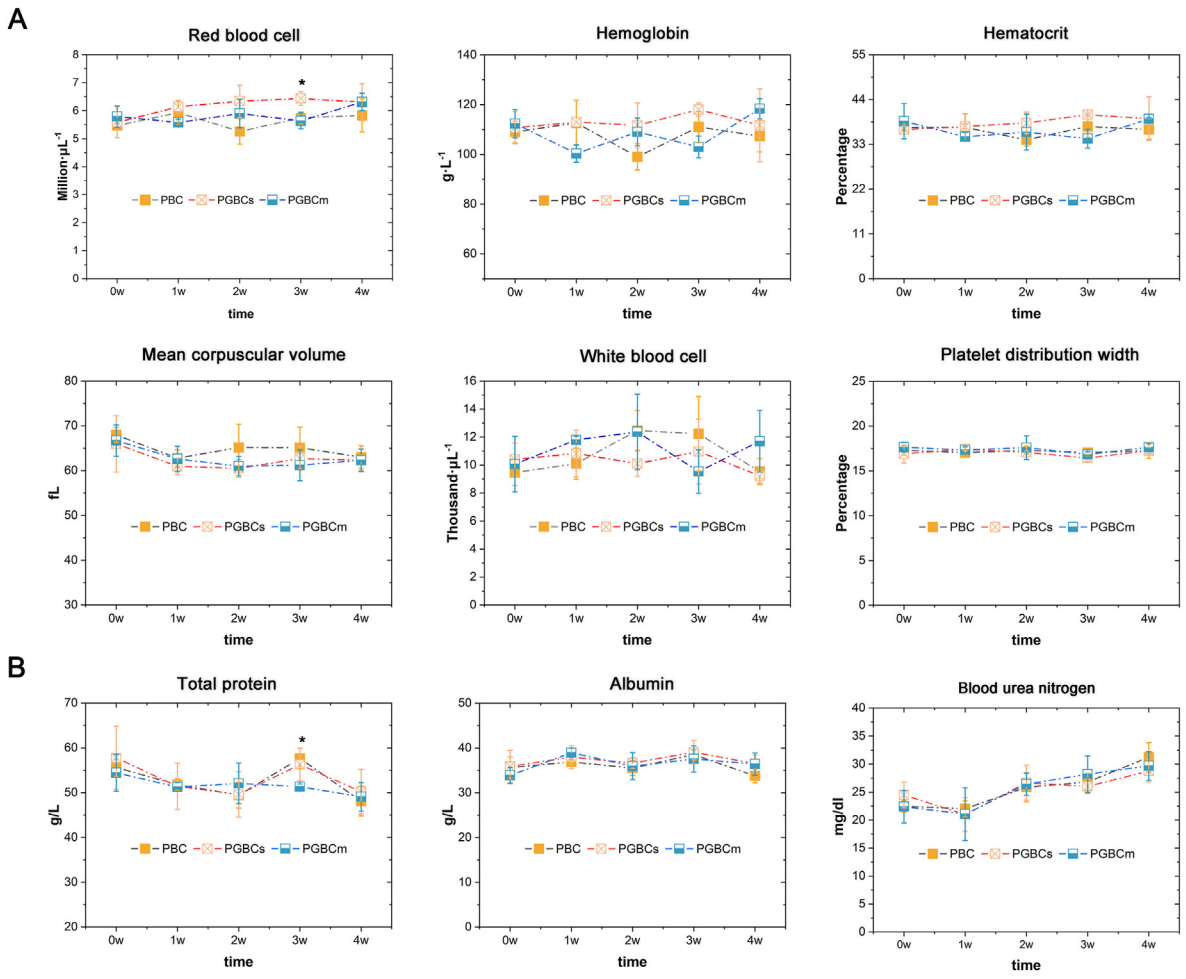

Fig. 7. Haematological and biochemical testing of rabbits after bone cement implantation. (n = 3, * indicates P < 0.05 compared to the PBC group; #P < 0.05 compared to the PGBCs group. Data are presented as the mean ± standard deviation).

between the aromatic rings of St and GO and the formation of ester bonds between AA and GO were the probable interaction between GO and P(MMA-AA-St) [61–63]. These mechanisms have been illustrated in Fig. 1C. The TEM morphology of P(MMA-AA-St)-GO nanocomposites further demonstrated that GO wrapped well around the P(MMA-AA-St) nanoparticles.

The water absorption capability of P(MMA-AA-St) was markedly improved after GO incorporation, which might be attributable to the inherent hydrophilicity of GO and the increased porosity of the material. GO incorporation has been reported to increase the porosity of modified cement [43]. This finding was also detected in PGBCs and PGBCm that their porosities and pore sizes were significantly higher than that of PBC. In addition, the porosity of PGBCs was also more significant than that of PGBCm. This might illustrated the superior water uptake capacity of PGBCs to PGBCm. The water-absorption ratio of PGBCs was 1.22-fold higher than that of PGBCm (95.14 ± 5.71% *vs.* 78.10 ± 2.60%). The method of GO incorporation may be responsible for this disparity. GO lamellae were distributed around the P(MMA-AA-St) nanoparticles in PGBCs, which allowed a larger surface for water contact during water absorption. In contrast, GO was directly mixed with P(MMA-AA-St) nanoparticles in PGBCm, allowing the possibility of self-aggregation. Therefore, GO was partially embedded during cement solidification and then caused a reduction in water contact, leading to a lower absorption ratio in PGBCm. In addition, the volume of PGBCs expanded 1.21-fold more than that of PGBCm (101.18 ± 5.31% *vs.* 83.36 ± 3.49%), which seemed to be consistent with the water absorption ratio. This result indicated that the volume expansion was positively correlated with the water absorption capability.

After the introduction of GO, by either synthesizing or mixing with P(MMA-AA-St), the compressive strengths of the resulting cements were superior to that of pure P(MMA-AA-St). This mechanical reinforcement by GO could be attributed to the characteristic structure of GO. The high surface area, wrinkled surface, and high quantity of superficial functional groups could facilitate a strong interfacial adhesion and/or interlocking between GO and the modified material through group-group interactions according to the previous reported studies [43,44,57]. Besides, the bridging effect achieved by GO incorporation could hinder crack propagation might be another reason for mechanical improvement [57]. Furthermore, π-π interactions, hydrogen bonding, and ester bonding formed between GO and P(MMA-AA-St) were reported to be the reason for the mechanical improvement [61]. Despite GO having been incorporated into both PGBCs and PGBCm, the compressive strength of PGBCm was inferior to that of PGBCs which might due to the different ways of GO addition. GO aggregation might play a role in impairing the biomechanical properties of its modified materials by creating mechanical weak points in the bone cement matrix [31,43]. Therefore, GO aggregation might be one of the factors attributed to the mechanical reduction of PGBCm when compared to PGBCs. While method of synthesizing GO with the P(MMA-AA-St) nanoparticles in the fabrication of PGBCs could overcome the drawbacks of simply mixing GO into the cement matrix, as mentioned above.

Both the compressive strengths of PGBCs before and after PBS

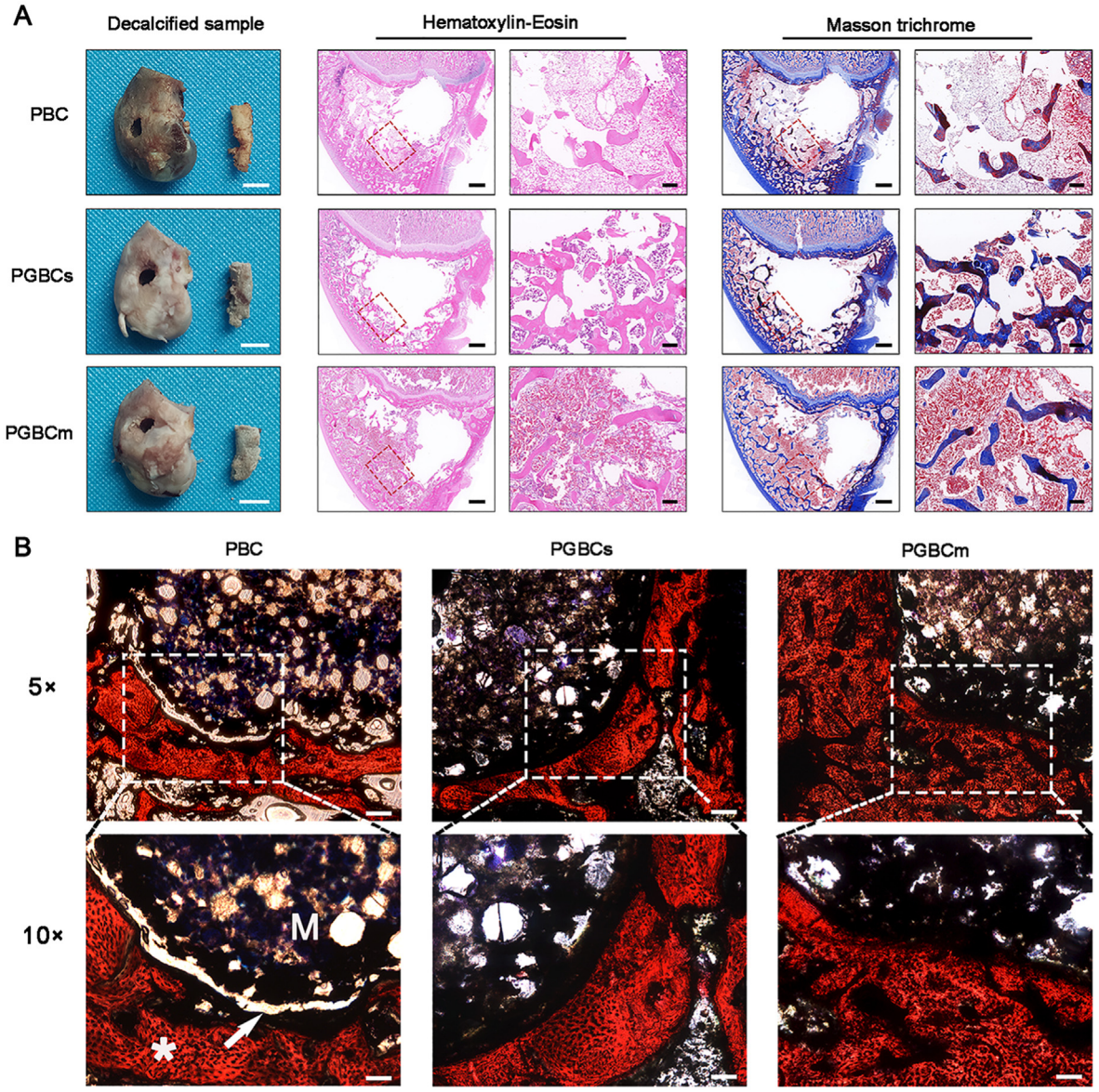

Fig. 8. Histological evaluation at different time points after material implantation. HE and Masson staining of a decalcified femoral condyle harvested four weeks after surgery (A). The defects formed after bone cement removal are the holes centred in the sections. The red square indicates the trabecular bone adjacent to the bone cement, and the blue-stained area indicates the synthesized collagen matrix. VG staining of the undecalcified femoral condyle harvested 16 weeks after surgery was performed to observe the bone-cement contact (B). A linear area of light transmission was detected at the bone-cement interface in the PBC group (white arrow); the letter "M" indicates the implanted material, and the symbol "*" indicates bone tissue, which was stained red. (n = 3. The scale bar of decalcified samples is 0.5 cm. The scale bar of images of HE and Masson's trichrome staining is 1 mm at 1 × magnification (left) and 200 μm at 5 × magnification (right); the scale bar of images of VG staining is 50 μm at 5 × magnification and 100 μm at 10 × magnification). (For interpretation of the references to color in this figure legend, the reader is referred to the Web version of this article.)

immersion exceeded the minimum requirement for that of acrylic bone cement (70 MPa), although they were lower than that of PBC. However, the compressive strength of PGBCm after immersion in PBS was approximately 60.20 MPa, which did not satisfy the standard. The higher compressive strength of PGBCs after PBS immersion further demonstrated that synthesis was a superior way of optimization than just mixing GO into P(MMA-AA-St). However, it is still worth noting that the standard protocol for compressive strength testing is performed using samples without PBS immersion. That means PGBCm still fitted the requirement of acrylic bone cement standard ISO 5833:2002. Furthermore, the elastic modulus of PGBCs and PGBCm was obviously lower than that of PBC. It has been reported that pore formation in PBC could reduce its elastic modulus [18]. This phenomenon was also detected in PGBCs and PGBCm using micro-CT scanning and the results demonstrated that porosities of them were higher than that of PBC. In summary, the mechanical properties of PGBCs, studied regardless of whether immersed in PBS or not, indicated that it may be safely used in orthopaedic surgery in the future.

High exothermic temperature-related bone necrosis is another concern in PBC applications. Both the T_{set} and T_{max} of PGBCs were significantly lower than those of PBC. In addition, the T_{set} and T_{max} of PGBCs were lower than those of PGBCm, although the difference was not statistically significant. Moreover, the t_{set} and t_{dough} of PGBCs were significantly longer than those of PBC, and the t_{set} of PGBCs was longer than that of PGBCm. Paz discovered that the addition of GO and G partially interfered with polymerization [43]. Retardation and inhibition were two postulated mechanisms by which the carbon nanostructures restricted PMMA polymerization, in which the aromatic ring played a

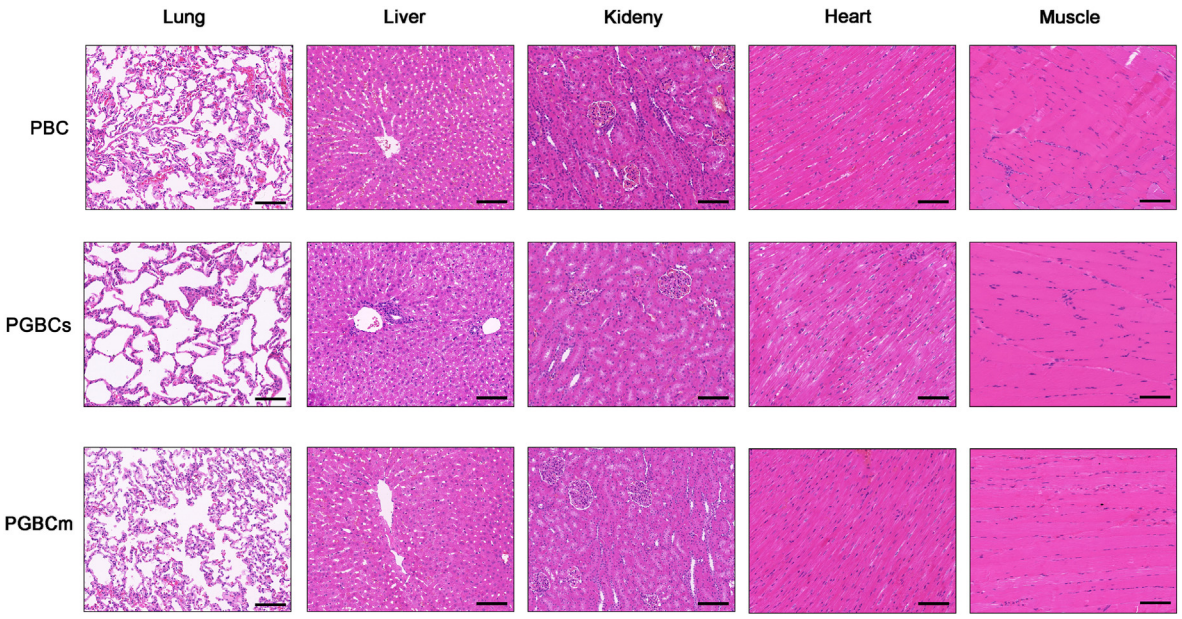

Fig. 9. HE staining of muscles adjacent to the site of bone cement implantation and organs harvested four weeks after surgery. No obvious morphological differences were detected among the groups in the lungs, liver, kidneys, heart, or muscle. (n = 3. The scale bar is 100 μm).

crucial role [44]. In retardation, the initiation activity of polymerization would be partially lost because the primary radicals generated from the BPO split could interact with the aromatic ring of the carbon nanostructures and then lose their coupling electrons. In inhibition, the polymer chain growth would be terminated because the aromatic ring might undergo electron transference during the growth of macromolecular radicals. These two mechanisms might occur in the polymerization of PGBCs and PGBCm. Moreover, the content of BPO was reduced by half in PGBCs and PGBCm because 50% of the solid phase was replaced with P(MMA-AA-St)-GO or P(MMA-AA-St)\GO nanocomposite. As a result, the vigorous polymerization was relieved after the introduction of GO into PGBCs and PGBCm. Consequently, the T_{set} and T_{max} of PGBCs were significantly lower than those of PBC, and the t_{dough} and t_{set} of PGBCs and PGBCm were still longer than those of PBC. This was consistent with the previously reported changes after the modification of PBC with GO [43, 61].

Furthermore, polyacrylic acid has been reported to have better thermal conductivity than PMMA, which was correlated with water uptake and hydrogen bonding [64]. In addition, GO is a thermal conductive material [65] which could improve the thermal conductivity of polyvinyl alcohol up to 50-fold [66]. Therefore, it is theoretically true that the effective thermal conductivity of AA and GO in PGBCs and PGBCm could improve heat dissipation to relieve the effect of bone necrosis resulting from the exotherm of PBC polymerization. The results of T_{set} and T_{max} of PGBCs and PGBCm coincided with this theoretical postulation. In particular, the decrease in T_{max} would relieve the thermal necrosis effect of PBC while benefiting bone-cement integration. Additionally, the adequate extension of t_{dough} and t_{set} would provide a surgeon with more manipulation time during operation. Above all, the chemical and mechanical properties of PGBCs and PGBCm were improved after modification with GO. In addition, PGBCs showed greater water absorption and volume expansion than PGBCm while exhibiting better mechanics and curing properties.

The PGBCs and PGBCm groups exhibited better cell viability than the PBC group, as demonstrated by the CCK-8 assay and live/dead staining assay. The toxicity of PBC mainly originates from unreacted MMA monomers and residual radicals [19]. As discussed above, the incorporation of GO in PGBCs and PGBCm could retard polymerization and prolong the curing time, allowing a sufficient solid–liquid phase reaction to reduce the residual monomer content. Besides, GO could react with MMA in the liquid phase at a hydrogen position via esterification [67]. Furthermore, due to the content of BPO being reduced by half in PGBCs and PGBCm and the incorporated GO acting as a radical scavenger [44, 67], the level of BPO split-related radicals would also be reduced. This reduction might be the reason for the lower cytotoxicity of PGBCs and PGBCm compared to PBC. This finding is supported by Pahlevanzadeh's and Tavakoli's studies, in which GO modification was suggested to improve the cytocompatibility of PBC [34,61]. In addition, the results further indicated superior cell viability in the PGBCs group compared to that in the PGBCm group. This could be attributed to the fact that the GO in PGBCs could intervene in polymerization more than the GO in PGBCm. The better cell viability in the PGBCs group was further illustrated by live/dead cell staining after osteoblasts were treated with the three materials (Fig. 4B and C). Furthermore, the 4-day osteoblast apoptosis rate was better after culture with PGBCs extract than PBC extract, and the 7-day osteoblast apoptosis rate was better in the PGBCs group than in the PBC and PGBCm groups. This was consistent with the reported apoptosis rate of 2.2% when Sao-2 osteoblasts were cultured with GO-modified PBC [45]. Despite the cytocompatibility of PGBCs and PGBCm was proven to be better than that of PBC in the present study, and obtained polymerized crude products of P(MMA-AA-St)-GO and P(MMA-AA-St) were washed to eliminate AA and St monomers, the method to improve the rate of polymerization to reduce the risk of AA and St leakage needs further consideration, especially when they were intended to translate in clinical use.

Cell attachment initiates cell biomaterial recognition and plays a primary role in the subsequent cellular response. The quality of cell adhesion influences the morphology, proliferation, and differentiation of the attached cells on biomaterials [45]. In this study, SEM indicated that osteoblasts were prone to better adhesion on the surface of PGBCs and PGBCm than on the surface of PBC, with cells on the PGBCs surface exhibiting the best spreading. This was in accordance with reported findings that a rougher surface and greater wettability are beneficial for osteoblast growth on bone cement [26,33]. In addition to the pronounced water absorption capacity of PGBCs and PGBCm, the coral-like surface of these materials is obviously rougher than that of PBC (Fig. 5A) and similar to the surface of P(MMA-AA-St) bone cement, as observed in our previous study [35]. Therefore, these factors might induce better cell spreading on PGBCs and PGBCm surfaces, and these results were consistent with those of a reported study related to GO-modified bone

cement [34].

GO could also act as a preconcentration platform for serum proteins, as it has been found to absorb up to 25% of serum proteins after being dispersed in FBS for one day [37]. It has been reported that the sp^2 carbon domains [68], π-π interactions, and electrostatic and hydrogen bonding of GO play important roles in protein preconcentration [37] (**Graphical abstract**) and are regarded as contributing factors to the enhancement of cell growth and induction of osteogenic differentiation by GO. In addition, the abundance of oxygen-containing functional groups on the GO surface could conjugate with other functional entities (chemicals and growth factors) to accelerate cell proliferation and differentiation [69]. Therefore, the results of better osteoblast attachment and proliferation in PGBCs and PGBCm groups illustrated that they might also be capable of protein concentration to further facilitate the attachment, proliferation, and differentiation of osteoblasts.

Reported studies have indicated that PBC could downregulate the expression of osteogenic genes such as *Alp*, *Ocn*, and *Runx2* [24,70]. While this downregulation could be attenuated by the modification of PBC with GO [71]. In addition, PBC inhibits osteoblast differentiation through the bone morphogenetic protein (BMP) signalling pathway using p38 MAPK as a downstream effector [72]. As previously reported, GO could enhance the osteogenic capability of its modified materials [36,37,39]. This effect was also detected in PGBCs and PGBCm. The qRT–PCR results demonstrated that the *Opn* expression level was higher in osteoblasts cultured on PGBCs and PGBCm than in osteoblasts cultured on PBC (Fig. 5B). *Opn* is not only an osteogenic marker but also a regulator of the osteoblast adhesion [73]. These higher expression levels detected in the PGBCs and PGBCm groups seem to be consistent with the greater cell spreading of the osteoblasts attached to PGBCs and PGBCm that was observed by SEM (Fig. 5A). Besides, higher *Alp* expression in cells cultured on PGBCs might indicate that PGBCs has a superior osteogenic capability compared to PGBCm and PBC. Smad5 is a transcription factor in the Smad family that transduces BMP signals into the nucleus to promote osteoblast maturation [74]. The level of Smad5 in the PGBCs group was higher than that in the other two groups, further indicating that PGBCs could facilitate bone formation (Fig. 5B). This finding coincides with that of a previous study demonstrating that GO could promote osteogenesis by enhancing BMP-Smad1/5 signal transduction [75]. The protein expression detected by Western blot analysis was approximately consistent with the gene expression noted above. This further demonstrated that the GO-modified PGBCs and PGBCm had a greater osteogenic capability than PBC (Fig. 5C). In summary, the *in vitro* osteoblast coculture results indicate better cell-material interactions and greater osteogenic capability in the PGBCs and PGBCm groups than in the PBC group.

The greater osteogenic capability of PGBCs and PGBCm was further demonstrated by the results of HE, Masson trichrome, and VG staining and microstructural analysis which indicated the osteointegration in this study. Both the trabecular number and thickness, as well as the bone formation potential, as indicated by collagen matrix synthesis [76], were superior in the PGBCs and PGBCm groups compared to those in the PBC group (Fig. 8A). The lower trabecular number and thickness detected in the PBC group might be correlated with thermal necrosis due to the high exothermic temperature during the polymerization [77]. In addition, the lower degree of collagen matrix synthesis might be attributed to the toxicity of PBC, which has been discussed above. First, the difference in the peri-implant microenvironment created around bone tissue might be a factor affecting osteointegration after material implantation. Due to the pronounced water absorption capability of PGBCs and PGBCm, the surrounding bone tissue might be prone to grow better in these two groups than in the hydrophobic PBC group. Second, the lower toxicity of PGBCs and PGBCm could facilitate osteoblast attachment and proliferation. Therefore, creating a better cell-material interaction which could further improve osteointegration Third, the ability of GO to enhance osteogenesis could further promote the anabolic activity of osteoblasts, which has been demonstrated at the cell and tissue levels. HE and Masson trichrome staining performed four weeks after surgery revealed an early stage of bone repair, while VG staining performed at 16 weeks revealed a late stage of bone-cement interaction after bone repair (Fig. 8B). An obvious linear space between the bone and cement was observed in the PBC group. This crack might have been generated by volumetric shrinkage and the inferior biocompatibility and osteointegration capability of PBC due to its inertness.

The results of the histological evaluation were further supported by the microstructural analysis performed using micro-CT reconstruction at 4 and 16 weeks after surgery. The BV/TV results indicated a larger volume of regenerated bone around the PGBCs than around the PBC and PGBCm. In addition, more trabeculae (Tb.N) were distributed around the PGBCs than the PBC and PGBCm, and the distance between trabeculae (Tb.Sp) was smaller in the PGBCs group than in the PBC and PGBCm groups. The microstructural analysis indicated that bone repair proceeded better after bone defects were filled with PGBCs (Fig. 6I-N). This superior osseointegration of PGBCs could be correlated with GO incorporation and was consistent with observations in previous studies [78,79].

It has been reported that the leakage of PBC monomers into the blood is considered to be the aetiology of BCIS [20,21]. Haematological, biochemical and histological assays of the main organs and muscle surrounding the material were performed to evaluate the biosafety of PGBCs and PGBCm (Figs. 7 and 9 and Fig. S4). The results revealed no differences among the groups in either haematological or biochemical parameters except the RBC count and TP at 3 weeks, which might be attributed to individual differences. In addition, no obvious disparities were found in the histological morphology of the critical organs of rabbits in the three groups by HE staining. Therefore, both blood and histological assays indicated that the biosafety of PGBCs and PGBCm was at least equal to that of PBC. In summary, while the *in vivo* study demonstrated satisfactory biosafety for both PGBCs and PGBCm, the histomorphological and microstructural analyses indicated better osteointegration for PGBCs than PGBCm.

$BaSO_4$ is a common radiopacifier in acrylic bone cement and the radiopacity increases with its content [80,81]. The $BaSO_4$ of PGBCs and PGBCm was half-reduced when compared to PBC while their radio radiopacity was normal (Fig. 6). Whether this reduction could affect the physicochemical and biological properties is another concern in developing PGBCs and PGBCm. Acrylic bone cement containing 10% $BaSO_4$ had superior mechanics to the plain counterpart [82]. In addition, the compressive load was comparable among acrylic bone cements with $BaSO_4$ ranging from 10% to 30% except that was reduced in the 40% one. But the bending strength and impact load gradually decreased as the content of $BaSO_4$ increased [80]. This finding was in accordance with that of a mechanical study in which KyphX HV-R (30%) had comparable or superior mechanics to neat Simplex P (10%). However, adding $BaSO_4$ directly to Simplex P lowered the tensile strength and fatigue life of the resulting cement (36.6%) [83]. The agglomerations of $BaSO_4$ were thought to be responsible for the local geometric stress concentrations, initiate cracks, and thereafter impair the mechanics of commercial CMW-1 (9.10%) [84]. And more scattered agglomerate formation has been discovered in Spineplex (30%) when compared to Simplex (10%) despite the former having a superior radiopacity [81]. In addition, adding extra $BaSO_4$ in neat Simplex P could facilitate the formation of large agglomerations and thereafter lower mechanical properties of the resulted cement (36.6%) by the mechanism mentioned above [83]. The formation of the $BaSO_4$ agglomeration seemed positively correlated to the concentration of $BaSO_4$. Therefore, the reduced content of $BaSO_4$ might benefit the mechanics of PGBCs and PGBCm.

It had been discovered that acrylic bone cement with 10% $BaSO_4$ possessed better osteoblast compatibility than its plain counterpart [82]. Besides, early studies demonstrated that adding $BaSO_4$ into acrylic bone cement was safe and could not provoke an inflammatory response, however, a later study indicated that Simplex P (10%) would induce greater leukocyte recruitment and inflammatory mediators release *in*

vitro and *in vivo*, and a greater osteolytic effect was observed when comparing to the Simplex Plain (0%) [85]. These findings were in accordance with the discoveries that additive $BaSO_4$ (9.2%–10%) could activate bone resorption and increase the cytokine TNF-α release no matter what size of the particles was 1 μm or 10 μm [86]. Besides, the foreign-body giant cells and mononuclear macrophages were also discovered around Simplex (10%) in the augmented human vertebral bodies [87]. While another *in vivo* histological analysis of the augmented sheep vertebrate revealed that foreign-body giant cells were found around Spineplex (30%) but few particles were discovered around Simplex (10%). It seemed that acrylic bone cement with fewer $BaSO_4$ have better tissue compatibility than its counterpart with more $BaSO_4$ [81]. In conclusion, $BaSO_4$ could facilitate osteoblast-bone cement interaction, however, it could also stimulate the activity of osteoclast and inflammatory cells in a dose-dependent manner probably. Therefore, the reduced content of $BaSO_4$ might benefit the biological properties of PGBCs and PGBCm. Due to acrylic bone cement being a multi-component product, the effects of different components on its physicochemical and biological properties might be overlapped [88]. Using radiolucent acrylic cement might be a way to detect the influence of $BaSO_4$ concentrations on the mechanical and biological effects of the optimized PMMA-based bone cement in the future.

This study demonstrates that GO-modified PGBCs has remarkable biological properties and partially overcomes the drawbacks of traditional PBC by exhibiting reduced toxicity, improved biomechanics, and enhanced biocompatibility. In addition, further investigation is needed to determine the effect of the protein preconcentration of PGBCs, which is thought to be the mechanism of its improved cytocompatibility but has only theoretical support in published studies. Meanwhile, PGBCs is a nondegradable biomaterial, and the lasting effect of its retention in the body could not be detected, warranting further investigation. Furthermore, the samples in this study were prepared using hand-mixed cement, while the vacuum-mixing technique has been used in surgical practice. Therefore, the vacuum-mixing technique should be applied in the future to prevent bias in sample preparation and more commercial PBC products should be compared to evaluate the properties of PGBCs. Finally, while the advantages of PGBCs make it attractive for clinical translation, a tremendous amount of work is still required to refine PGBCs (or its derivatives) to render it suitable for clinical translation, whereas commercial PBC has been applied in the clinic for decades.

5. Conclusions

This study reported PGBCs, a self-expandable hydrophilic and osteogenic composite exhibiting improved biomechanics and preserved outstanding water uptake and volumetric expansion properties by synthesis with GO. This modified material also showed a lower polymerizing temperature and longer handling time. In addition, the biocompatibility and osteogenic capability were assessed *in vitro* and *in vivo* and found to be better than those of PBC due to the hydrophilicity and osteoinductive effect of GO incorporation. Furthermore, no obvious disparities related to biosafety were detected between PGBCs and PBC. Therefore, PGBCs largely overcomes the drawbacks of conventionally used PBC, including the volumetric shrinkage, high elastic modulus, toxicity, and poor osseointegration. Additionally, the results also indicated that synthesis rather than mixing with GO was the superior method for GO modification in this study. The findings of this study can provide new insight into the research, development, and clinical translation of bone-filling materials.

Credit author statement

Quan-Chang Tan: Conceptualization, Methodology, Investigation, Data curation, Formal analysis, Visualization, Writing – original draft, Writing – review & editing; Xia-Shu Jiang: Methodology, Investigation, Data curation; Lei Chen: Methodology, Investigation; Jin-Feng Huang: Investigation, Data curation; Qiu-Xia Zhou: Investigation; Jing Wang: Methodology; Yan Zhao: Investigation; Bo Zhang: Methodology, Investigation; Ya-Ni Sun: Investigation; Min Wei: Investigation; Xiong Zhao: Methodology; Zhao Yang: Funding acquisition; Writing – review & editing. Wei Lei: Project administration, Supervision; Writing – review & editing; Yu-Fei Tang: Project administration, Supervision, Writing – review & editing; Zi-Xiang Wu: Project administration, Funding acquisition, Supervision, Writing – review & editing.

Declaration of competing interest

The authors declare that they have no known competing financial interests or personal relationships that could have appeared to influence the work reported in this paper.

Data availability

Data will be made available on request.

Acknowledgements

This work was supported by the National Natural Science Foundation of China (No. 81772310 and No. 81902185), Shaanxi Province Key Research and Development Projects (No. 2021SF-175), and China Postdoctoral Science Foundation (2020M673661). The funding source did not influence the study design, collection, analysis, or interpretation of data. The original crystal structures of fibronectin and albumin in Graphical Abstract were downloaded from Protein Data Bank and reconstructed and visualized with open software PyMol.

Appendix A. Supplementary data

Supplementary data to this article can be found online at https://doi.org/10.1016/j.mtbio.2022.100500.

References

[1] S. Sebastian, Y. Liu, R. Christensen, D.B. Raina, M. Tägil, L. Lidgren, Antibiotic containing bone cement in prevention of hip and knee prosthetic joint infections: a systematic review and meta-analysis, J Orthop Translat 23 (2020) 53–60, https://doi.org/10.1016/j.jot.2020.04.005.

[2] P. van der Voort, E.R. Valstar, B.L. Kaptein, M. Fiocco, H.J. van der Heide, R.G. Nelissen, Comparison of femoral component migration between Refobacin bone cement R and Palacos R + G in cemented total hip arthroplasty: a randomised controlled roentgen stereophotogrammetric analysis and clinical study, Bone Joint Lett. J 98-b (10) (2016) 1333–1341, https://doi.org/10.1302/0301-620x.98b10.37116.

[3] O. Robertsson, J. Ranstam, M. Sundberg, W.D. A, L. Lidgren, The Swedish knee arthroplasty register: a review, Bone Joint Res 3 (7) (2014) 217–222, https://doi.org/10.1302/2046-3758.37.2000289.

[4] M.J. Nieuwenhuijse, A.R. Van Erkel, P.D. Dijkstra, Cement leakage in percutaneous vertebroplasty for osteoporotic vertebral compression fractures: identification of risk factors, Spine J. : official journal of the North American Spine Society 11 (9) (2011) 839–848, https://doi.org/10.1016/j.spinee.2011.07.027.

[5] M.H. Hu, H.T. Wu, M.C. Chang, W.K. Yu, S.T. Wang, C.L. Liu, Polymethylmethacrylate augmentation of the pedicle screw: the cement distribution in the vertebral body, Eur. Spine J. : official publication of the European Spine Society, the European Spinal Deformity Society, and the European Section of the Cervical Spine Research Society 20 (8) (2011) 1281–1288, https://doi.org/10.1007/s00586-011-1824-4.

[6] M.P. Patel, M. Braden, K.W. Davy, Polymerization shrinkage of methacrylate esters, Biomaterials 8 (1) (1987) 53–56, https://doi.org/10.1016/0142-9612(87)90030-5.

[7] J.L. Gilbert, J.M. Hasenwinkel, R.L. Wixson, E.P. Lautenschlager, A theoretical and experimental analysis of polymerization shrinkage of bone cement: a potential major source of porosity, J. Biomed. Mater. Res. 52 (1) (2000) 210–218, https://doi.org/10.1002/1097-4636(200010)52:1<210::aid-jbm27>3.0.co;2-r.

[8] F.N. Kwong, R.A. Power, A comparison of the shrinkage of commercial bone cements when mixed under vacuum, J Bone Joint Surg Br 88 (1) (2006) 120–122, https://doi.org/10.1302/0301-620x.88b1.16600.

[9] S.S. Haas, G.M. Brauer, G. Dickson, A characterization of polymethylmethacrylate bone cement, the Journal of bone and joint surgery, American volume 57 (3) (1975) 380–391.

[10] A. Roques, M. Browne, A. Taylor, A. New, D. Baker, Quantitative measurement of the stresses induced during polymerisation of bone cement, Biomaterials 25 (18) (2004) 4415–4424, https://doi.org/10.1016/j.biomaterials.2003.11.009.

[11] S. Griza, M.M. Ueki, D.H. Souza, A. Cervieri, T.R. Strohaecker, Thermally induced strains and total shrinkage of the polymethyl-methacrylate cement in simplified models of total hip arthroplasty, J. Mech. Behav. Biomed. Mater. 18 (2013) 29–36, https://doi.org/10.1016/j.jmbbm.2012.09.018.
[12] M. Atai, D.C. Watts, Z. Atai, Shrinkage strain-rates of dental resin-monomer and composite systems, Biomaterials 26 (24) (2005) 5015–5020, https://doi.org/10.1016/j.biomaterials.2005.01.022.
[13] M.A. Miller, J.R. Goodheart, B. Khechen, D. Janssen, K.A. Mann, Changes in microgaps, micromotion, and trabecular strain from interlocked cement-trabecular bone interfaces in total knee replacements with in vivo service, J. Orthop. Res. : official publication of the Orthopaedic Research Society 34 (6) (2016) 1019–1025, https://doi.org/10.1002/jor.23109.
[14] M. Kinzl, A. Boger, P.K. Zysset, D.H. Pahr, The mechanical behavior of PMMA/bone specimens extracted from augmented vertebrae: a numerical study of interface properties, PMMA shrinkage and trabecular bone damage, J. Biomech. 45 (8) (2012) 1478–1484, https://doi.org/10.1016/j.jbiomech.2012.02.012.
[15] S. Takahashi, M. Hoshino, H. Yasuda, Y. Hori, S. Ohyama, H. Terai, K. Hayashi, T. Tsujio, H. Kono, A. Suzuki, K. Tamai, H. Toyoda, S. Dohzono, R. Sasaoka, F. Kanematsu, H. Nakamura, Development of a scoring system for predicting adjacent vertebral fracture after balloon kyphoplasty, Spine J. : official journal of the North American Spine Society 19 (7) (2019) 1194–1201, https://doi.org/10.1016/j.spinee.2019.02.013.
[16] J. Zhu, K. Zhang, K. Luo, Z. Qiu, S. Yang, F. Cui, X. Weng, G. Jiang, Mineralized collagen modified polymethyl methacrylate bone cement for osteoporotic compression vertebral fracture at 1-year follow-up, Spine 44 (12) (2019) 827–838, https://doi.org/10.1097/brs.0000000000002971.
[17] C. Robo, C. Öhman-Mägi, C. Persson, Long-term mechanical properties of a novel low-modulus bone cement for the treatment of osteoporotic vertebral compression fractures, J. Mech. Behav. Biomed. Mater. 118 (2021), 104437, https://doi.org/10.1016/j.jmbbm.2021.104437.
[18] A. Boger, M. Bohner, P. Heini, K. Schwieger, E. Schneider, Performance of vertebral cancellous bone augmented with compliant PMMA under dynamic loads, Acta Biomater. 4 (6) (2008) 1688–1693, https://doi.org/10.1016/j.actbio.2008.06.019.
[19] A. Hoess, A. López, H. Engqvist, M.K. Ott, C. Persson, Comparison of a quasi-dynamic and a static extraction method for the cytotoxic evaluation of acrylic bone cements, Mater Sci Eng C Mater Biol Appl 62 (2016) 274–282, https://doi.org/10.1016/j.msec.2016.01.048.
[20] E. Schwarzkopf, R. Sachdev, J. Flynn, V. Boddapati, R.E. Padilla, D.E. Prince, Occurrence, risk factors, and outcomes of bone cement implantation syndrome after hemi and total hip arthroplasty in cancer patients, J. Surg. Oncol. 120 (6) (2019) 1008–1015, https://doi.org/10.1002/jso.25675.
[21] J. Modig, C. Busch, S. Olerud, T. Saldeen, G. Waernbaum, Arterial hypotension and hypoxaemia during total hip replacement: the importance of thromboplastic products, fat embolism and acrylic monomers, Acta Anaesthesiol. Scand. 19 (1) (1975) 28–43, https://doi.org/10.1111/j.1399-6576.1975.tb05219.x.
[22] M. Choppadandi, N. More, G. Kapusetti, Detoxification of poly(methyl methacrylate) bone cement by natural antioxidant intervention, J. Biomed. Mater. Res. 107 (12) (2019) 2835–2847, https://doi.org/10.1002/jbm.a.36785.
[23] N. Tsukimura, M. Yamada, H. Aita, N. Hori, F. Yoshino, M. Chang-Il Lee, K. Kimoto, A. Jewett, T. Ogawa, N-acetyl cysteine (NAC)-mediated detoxification and functionalization of poly(methyl methacrylate) bone cement, Biomaterials 30 (20) (2009) 3378–3389, https://doi.org/10.1016/j.biomaterials.2009.02.043.
[24] H. Aita, N. Tsukimura, M. Yamada, N. Hori, K. Kubo, N. Sato, H. Maeda, K. Kimoto, T. Ogawa, N-acetyl cysteine prevents polymethyl methacrylate bone cement extract-induced cell death and functional suppression of rat primary osteoblasts, J. Biomed. Mater. Res. 92 (1) (2010) 285–296, https://doi.org/10.1002/jbm.a.32336.
[25] K. Hamajima, R. Ozawa, J. Saruta, M. Saita, H. Kitajima, S.R. Taleghani, D. Usami, D. Goharian, M. Uno, K. Miyazawa, S. Goto, K. Tsukinoki, T. Ogawa, The effect of TBB, as an initiator, on the biological compatibility of PMMA/MMA bone cement, Int. J. Mol. Sci. 21 (11) (2020), https://doi.org/10.3390/ijms21114016.
[26] Y. Sugita, T. Okubo, M. Saita, M. Ishijima, Y. Torii, M. Tanaka, C. Iwasaki, T. Sekiya, M. Tabuchi, N. Mohammadzadeh Rezaei, T. Taniyama, N. Sato, J. Saruta, M. Hasegawa, M. Hirota, W. Park, M.C. Lee, H. Maeda, T. Ogawa, Novel osteogenic behaviors around hydrophilic and radical-free 4-META/MMA-TBB: implications of an osseointegrating bone cement, Int. J. Mol. Sci. 21 (7) (2020), https://doi.org/10.3390/ijms21072405.
[27] C. Wolf-Brandstetter, S. Roessler, S. Storch, U. Hempel, U. Gbureck, B. Nies, S. Bierbaum, D. Scharnweber, Physicochemical and cell biological characterization of PMMA bone cements modified with additives to increase bioactivity, J. Biomed. Mater. Res. B Appl. Biomater. 101 (4) (2013) 599–609, https://doi.org/10.1002/jbm.b.32862.
[28] A.H. Phakatkar, M.R. Shirdar, M.L. Qi, M.M. Taheri, S. Narayanan, T. Foroozan, S. Sharifi-Asl, Z. Huang, M. Agrawal, Y.P. Lu, R. Shahbazian-Yassar, T. Shokuhfar, Novel PMMA bone cement nanocomposites containing magnesium phosphate nanosheets and hydroxyapatite nanofibers, Mater Sci Eng C Mater Biol Appl 109 (2020), 110497, https://doi.org/10.1016/j.msec.2019.110497.
[29] M. Miola, M. Bruno, G. Maina, G. Fucale, G. Lucchetta, E. Vernè, Antibiotic-free composite bone cements with antibacterial and bioactive properties. A preliminary study, Mater Sci Eng C Mater Biol Appl 43 (2014) 65–75, https://doi.org/10.1016/j.msec.2014.06.026.
[30] E. Verné, M. Bruno, M. Miola, G. Maina, C. Bianco, A. Cochis, L. Rimondini, Composite bone cements loaded with a bioactive and ferrimagnetic glass-ceramic: leaching, bioactivity and cytocompatibility, Mater Sci Eng C Mater Biol Appl 53 (2015) 95–103, https://doi.org/10.1016/j.msec.2015.03.039.
[31] Z.M. Wright, A.M. Pandit, M.M. Karpinsky, B.D. Holt, E.P. Zovinka, S.A. Sydlik, Bioactive, ion-releasing PMMA bone cement filled with functional graphenic materials, Adv Healthc Mater 10 (2) (2021), e2001189, https://doi.org/10.1002/adhm.202001189.
[32] S.B. Kim, Y.J. Kim, T.L. Yoon, S.A. Park, I.H. Cho, E.J. Kim, I.A. Kim, J.W. Shin, The characteristics of a hydroxyapatite-chitosan-PMMA bone cement, Biomaterials 25 (26) (2004) 5715–5723, https://doi.org/10.1016/j.biomaterials.2004.01.022.
[33] L.C. Lin, S.J. Chang, S.M. Kuo, S.F. Chen, C.H. Kuo, Evaluation of chitosan/beta-tricalcium phosphate microspheres as a constituent to PMMA cement, J. Mater. Sci. Mater. Med. 16 (6) (2005) 567–574, https://doi.org/10.1007/s10856-005-0533-0.
[34] F. Pahlevanzadeh, H.R. Bakhsheshi-Rad, E. Hamzah, In-vitro biocompatibility, bioactivity, and mechanical strength of PMMA-PCL polymer containing fluorapatite and graphene oxide bone cements, J. Mech. Behav. Biomed. Mater. 82 (2018) 257–267, https://doi.org/10.1016/j.jmbbm.2018.03.016.
[35] Z. Yang, L. Chen, Y. Hao, Y. Zang, X. Zhao, L. Shi, Y. Zhang, Y. Feng, C. Xu, F. Wang, X. Wang, B. Wang, C. Liu, Y. Tang, Z. Wu, W. Lei, Synthesis and characterization of an injectable and hydrophilous expandable bone cement based on poly(methyl methacrylate), ACS Appl. Mater. Interfaces 9 (46) (2017) 40846–40856, https://doi.org/10.1021/acsami.7b12983.
[36] Y. Luo, H. Shen, Y. Fang, Y. Cao, J. Huang, M. Zhang, J. Dai, X. Shi, Z. Zhang, Enhanced proliferation and osteogenic differentiation of mesenchymal stem cells on graphene oxide-incorporated electrospun poly(lactic-co-glycolic acid) nanofibrous mats, ACS Appl. Mater. Interfaces 7 (11) (2015) 6331–6339, https://doi.org/10.1021/acsami.5b00862.
[37] W.C. Lee, C.H. Lim, H. Shi, L.A. Tang, Y. Wang, C.T. Lim, K.P. Loh, Origin of enhanced stem cell growth and differentiation on graphene and graphene oxide, ACS Nano 5 (9) (2011) 7334–7341, https://doi.org/10.1021/nn202190c.
[38] T.H. Kim, S. Shah, L. Yang, P.T. Yin, M.K. Hossain, B. Conley, J.W. Choi, K.B. Lee, Controlling differentiation of adipose-derived stem cells using combinatorial graphene hybrid-pattern arrays, ACS Nano 9 (4) (2015) 3780–3790, https://doi.org/10.1021/nn5066028.
[39] Z. Zhang, Y. Wang, W. Teng, X. Zhou, Y. Ye, H. Zhou, H. Sun, F. Wang, A. Liu, P. Lin, W. Cui, X. Yu, Y. Wu, Z. Ye, An orthobiologics-free strategy for synergistic photocatalytic antibacterial and osseointegration, Biomaterials 274 (2021), 120853, https://doi.org/10.1016/j.biomaterials.2021.120853.
[40] J. Zhang, H. Eyisoylu, X.-H. Qin, M. Rubert, R. Müller, 3D bioprinting of graphene oxide-incorporated cell-laden bone mimicking scaffolds for promoting scaffold fidelity, osteogenic differentiation and mineralization, Acta Biomater. 121 (2021) 637–652, https://doi.org/10.1016/j.actbio.2020.12.026.
[41] Y. He, N. Zhang, Q. Gong, H. Qiu, W. Wang, Y. Liu, J. Gao, Alginate/graphene oxide fibers with enhanced mechanical strength prepared by wet spinning, Carbohydr. Polym. 88 (3) (2012) 1100–1108, https://doi.org/10.1016/j.carbpol.2012.01.071.
[42] M. Mehrali, E. Moghaddam, S.F.S. Shirazi, S. Baradaran, M. Mehrali, S.T. Latibari, H.S.C. Metselaar, N.A. Kadri, K. Zandi, N.A.A. Osman, Synthesis, mechanical properties, and in vitro biocompatibility with osteoblasts of calcium silicate–reduced graphene oxide composites, ACS Appl. Mater. Interfaces 6 (6) (2014) 3947–3962, https://doi.org/10.1021/am500845x.
[43] E. Paz, F. Forriol, J.C. Del Real, N. Dunne, Graphene oxide versus graphene for optimisation of PMMA bone cement for orthopaedic applications, Mater Sci Eng C Mater Biol Appl 77 (2017) 1003–1011, https://doi.org/10.1016/j.msec.2017.03.269.
[44] G. Gonçalves, S.M. Cruz, A. Ramalho, J. Grácio, P.A. Marques, Graphene oxide versus functionalized carbon nanotubes as a reinforcing agent in a PMMA/HA bone cement, Nanoscale 4 (9) (2012) 2937–2945, https://doi.org/10.1039/c2nr30303e.
[45] G. Gonçalves, M.T. Portolés, C. Ramírez-Santillán, M. Vallet-Regí, A.P. Serro, J. Grácio, P.A. Marques, Evaluation of the in vitro biocompatibility of PMMA/high-load HA/carbon nanostructures bone cement formulations, J. Mater. Sci. Mater. Med. 24 (12) (2013) 2787–2796, https://doi.org/10.1007/s10856-013-5030-2.
[46] E. Paz, Y. Ballesteros, J. Abenojar, J.C. Del Real, N.J. Dunne, Graphene oxide and graphene reinforced PMMA bone cements: evaluation of thermal properties and biocompatibility, Materials 12 (19) (2019), https://doi.org/10.3390/ma12193146.
[47] S. Marcia, E. Piras, J.A. Hirsch, A. Mereu, M. Marras, A. Spinelli, L. Saba, Efficacy of a novel vertebral body augmentation system in the treatment of patients with symptomatic vertebral body fractures, Cardiovasc. Intervent. Radiol. 44 (2) (2021) 289–299, https://doi.org/10.1007/s00270-020-02658-4.
[48] J. Zhu, S. Yang, K. Cai, S. Wang, Z. Qiu, J. Huang, G. Jiang, X. Wang, X. Fang, Bioactive poly (methyl methacrylate) bone cement for the treatment of osteoporotic vertebral compression fractures, Theranostics 10 (14) (2020) 6544–6560, https://doi.org/10.7150/thno.44428.
[49] I.R. Orriss, S.E. Taylor, T.R. Arnett, Rat osteoblast cultures, Methods Mol. Biol. 816 (2012) 31–41, https://doi.org/10.1007/978-1-61779-415-5_3.
[50] E. Jacobs, K. Saralidze, A.K. Roth, J.J. de Jong, J.P. van den Bergh, A. Lataster, B.T. Brans, M.L. Knetsch, I. Djordjevic, P.C. Willems, L.H. Koole, Synthesis and characterization of a new vertebroplasty cement based on gold-containing PMMA microspheres, Biomaterials 82 (2016) 60–70, https://doi.org/10.1016/j.biomaterials.2015.12.024.
[51] S.D. Purohit, R. Bhaskar, H. Singh, I. Yadav, M.K. Gupta, N.C. Mishra, Development of a nanocomposite scaffold of gelatin-alginate-graphene oxide for bone tissue engineering, Int. J. Biol. Macromol. 133 (2019) 592–602, https://doi.org/10.1016/j.ijbiomac.2019.04.113.
[52] G. Giavaresi, E. Bertazzoni Minelli, M. Sartori, A. Benini, A. Parrilli, M.C. Maltarello, F. Salamanna, P. Torricelli, R. Giardino, M. Fini, New PMMA-based composites for preparing spacer devices in prosthetic infections, J. Mater. Sci. Mater. Med. 23 (5) (2012) 1247–1257, https://doi.org/10.1007/s10856-012-4585-7.
[53] J. Wang, Y. An, F. Li, D. Li, D. Jing, T. Guo, E. Luo, C. Ma, The effects of pulsed electromagnetic field on the functions of osteoblasts on implant surfaces with

different topographies, Acta Biomater. 10 (2) (2014) 975–985, https://doi.org/10.1016/j.actbio.2013.10.008.
[54] L. Cao, J.A. Werkmeister, J. Wang, V. Glattauer, K.M. McLean, C. Liu, Bone regeneration using photocrosslinked hydrogel incorporating rhBMP-2 loaded 2-N, 6-O-sulfated chitosan nanoparticles, Biomaterials 35 (9) (2014) 2730–2742, https://doi.org/10.1016/j.biomaterials.2013.12.028.
[55] C. Yueyi, H. Xiaoguang, W. Jingying, S. Quansheng, T. Jie, F. Xin, X. Yingsheng, S. Chunli, Calvarial defect healing by recruitment of autogenous osteogenic stem cells using locally applied simvastatin, Biomaterials 34 (37) (2013) 9373–9380, https://doi.org/10.1016/j.biomaterials.2013.08.060.
[56] Q. Xie, Z. Wang, Y. Huang, X. Bi, H. Zhou, M. Lin, Z. Yu, Y. Wang, N. Ni, J. Sun, S. Wu, Z. You, C. Guo, H. Sun, Y. Wang, P. Gu, X. Fan, Characterization of human ethmoid sinus mucosa derived mesenchymal stem cells (hESMSCs) and the application of hESMSCs cell sheets in bone regeneration, Biomaterials 66 (2015) 67–82, https://doi.org/10.1016/j.biomaterials.2015.07.013.
[57] F. Pahlevanzadeh, H.R. Bakhsheshi-Rad, M. Kharaziha, M. Kasiri-Asgarani, M. Omidi, M. Razzaghi, A.F. Ismail, S. Sharif, S. RamaKrishna, F. Berto, CNT and rGO reinforced PMMA based bone cement for fixation of load bearing implants: mechanical property and biological response, J. Mech. Behav. Biomed. Mater. 116 (2021), 104320, https://doi.org/10.1016/j.jmbbm.2021.104320.
[58] M. Hazarika, T. Jana, Graphene nanosheets generated from sulfonated polystyrene/graphene nanocomposite, Compos. Sci. Technol. 87 (2013) 94–102, https://doi.org/10.1016/j.compscitech.2013.08.004.
[59] S. Li, T. Qian, S. Wu, J. Shen, A facile, controllable fabrication of polystyrene/graphene core-shell microspheres and its application in high-performance electrocatalysis, Chem Commun (Camb) 48 (64) (2012) 7997–7999, https://doi.org/10.1039/c2cc34411d.
[60] R. Wazalwar, N. Tripathi, A.M. Raichur, Mechanical and curing behavior of epoxy composites reinforced with polystyrene-graphene oxide (PS-GO) core-shell particles, Composites Part C: Open Access 5 (2021), 100128, https://doi.org/10.1016/j.jcomc.2021.100128.
[61] M. Tavakoli, S.S.E. Bakhtiari, S. Karbasi, Incorporation of chitosan/graphene oxide nanocomposite in to the PMMA bone cement: physical, mechanical and biological evaluation, Int. J. Biol. Macromol. 149 (2020) 783–793, https://doi.org/10.1016/j.ijbiomac.2020.01.300.
[62] Y. Huang, M. Zeng, J. Ren, J. Wang, L. Fan, Q. Xu, Preparation and swelling properties of graphene oxide/poly(acrylic acid-co-acrylamide) super-absorbent hydrogel nanocomposites, Colloids Surf. A Physicochem. Eng. Asp. 401 (2012) 97–106, https://doi.org/10.1016/j.colsurfa.2012.03.031.
[63] T. Zhang, X. Li, S. Kang, L. Qin, W. Yan, J. Mu, Facile assembly and properties of polystyrene microsphere/reduced graphene oxide/Ag composite, J. Colloid Interface Sci. 402 (2013) 279–283, https://doi.org/10.1016/j.jcis.2013.03.042.
[64] P. Hummel, A.M. Lechner, K. Herrmann, P. Biehl, C. Rössel, L. Wiedenhöft, F.H. Schacher, M. Retsch, Thermal transport in ampholytic polymers: the role of hydrogen bonding and water uptake, Macromolecules 53 (13) (2020) 5528–5537, https://doi.org/10.1021/acs.macromol.0c00596.
[65] X. Mu, X. Wu, T. Zhang, D.B. Go, T. Luo, Thermal transport in graphene oxide–from ballistic extreme to amorphous limit, Sci. Rep. 4 (2014) 3909, https://doi.org/10.1038/srep03909.
[66] X. Pan, M.G. Debije, A.P.H.J. Schenning, C.W.M. Bastiaansen, Enhanced thermal conductivity in oriented polyvinyl alcohol/graphene oxide composites, ACS Appl. Mater. Interfaces 13 (24) (2021) 28864–28869, https://doi.org/10.1021/acsami.1c06415.
[67] R.W. Ormsby, M. Modreanu, C.A. Mitchell, N.J. Dunne, Carboxyl functionalised MWCNT/polymethyl methacrylate bone cement for orthopaedic applications, J. Biomater. Appl. 29 (2) (2014) 209–221, https://doi.org/10.1177/0885328214521252.
[68] L. Wang, J. Qiu, J. Guo, D. Wang, S. Qian, H. Cao, X. Liu, Regulating the behavior of human gingival fibroblasts by sp2 domains in reduced graphene oxide, ACS Biomater. Sci. Eng. 5 (12) (2019) 6414–6424, https://doi.org/10.1021/acsbiomaterials.9b00497.
[69] J.-W. Yang, K.Y. Hsieh, P.V. Kumar, S.-J. Cheng, Y.-R. Lin, Y.-C. Shen, G.-Y. Chen, Enhanced osteogenic differentiation of stem cells on phase-engineered graphene oxide, ACS Appl. Mater. Interfaces 10 (15) (2018) 12497–12503, https://doi.org/10.1021/acsami.8b02225.
[70] R. Chiu, K.E. Smith, G.K. Ma, T. Ma, R.L. Smith, S.B. Goodman, Polymethylmethacrylate particles impair osteoprogenitor viability and expression of osteogenic transcription factors Runx2, osterix, and Dlx5, J. Orthop. Res. : official publication of the Orthopaedic Research Society 28 (5) (2010) 571–577, https://doi.org/10.1002/jor.21035.
[71] E.H. Mirza, A.A. Khan, A.A. Al-Khureif, S.A. Saadaldin, B.A. Mohamed, F. Fareedi, M.M. Khan, M. Alfayez, R. Al-Fotawi, P.K. Vallittu, A. Mahmood, Characterization of osteogenic cells grown over modified graphene-oxide-biostable polymers, Biomed. Mater. 14 (6) (2019), 065004, https://doi.org/10.1088/1748-605X/ab3ab2.
[72] G.K. Ma, R. Chiu, Z. Huang, J. Pearl, T. Ma, R.L. Smith, S.B. Goodman, Polymethylmethacrylate particle exposure causes changes in p38 MAPK and TGF-beta signaling in differentiating MC3T3-E1 cells, J. Biomed. Mater. Res. 94 (1) (2010) 234–240, https://doi.org/10.1002/jbm.a.32686.
[73] E.A. Mitchell, B.T. Chaffey, A.W. McCaskie, J.H. Lakey, M.A. Birch, Controlled spatial and conformational display of immobilised bone morphogenetic protein-2 and osteopontin signalling motifs regulates osteoblast adhesion and differentiation in vitro, BMC Biol. 8 (2010) 57, https://doi.org/10.1186/1741-7007-8-57.
[74] D.K. Kim, G. Bandara, Y.E. Cho, H.D. Komarow, D.R. Donahue, B. Karim, M.C. Baek, H.M. Kim, D.D. Metcalfe, A. Olivera, Mastocytosis-derived extracellular vesicles deliver miR-23a and miR-30a into pre-osteoblasts and prevent osteoblastogenesis and bone formation, Nat. Commun. 12 (1) (2021) 2527, https://doi.org/10.1038/s41467-021-22754-4.
[75] Z. Li, S. Xiang, Z. Lin, E.N. Li, H. Yagi, G. Cao, L. Yocum, L. Li, T. Hao, K.K. Bruce, M.R. Fritch, H. Hu, B. Wang, P.G. Alexander, K.A. Khor, R.S. Tuan, H. Lin, Graphene oxide-functionalized nanocomposites promote osteogenesis of human mesenchymal stem cells via enhancement of BMP-SMAD1/5 signaling pathway, Biomaterials 277 (2021), 121082, https://doi.org/10.1016/j.biomaterials.2021.121082.
[76] G. Xiang, K. Liu, T. Wang, X. Hu, J. Wang, Z. Gao, W. Lei, Y. Feng, T.H. Tao, In situ regulation of macrophage polarization to enhance osseointegration under diabetic conditions using injectable silk/sitagliptin gel scaffolds, Adv. Sci. 8 (3) (2021), 2002328, https://doi.org/10.1002/advs.202002328.
[77] Y. Lv, A. Li, F. Zhou, X. Pan, F. Liang, X. Qu, D. Qiu, Z. Yang, A novel composite PMMA-based bone cement with reduced potential for thermal necrosis, ACS Appl. Mater. Interfaces 7 (21) (2015) 11280–11285, https://doi.org/10.1021/acsami.5b01447.
[78] C. Zhou, S. Liu, J. Li, K. Guo, Q. Yuan, A. Zhong, J. Yang, J. Wang, J. Sun, Z. Wang, Collagen functionalized with graphene oxide enhanced biomimetic mineralization and in situ bone defect repair, ACS Appl. Mater. Interfaces 10 (50) (2018) 44080–44091, https://doi.org/10.1021/acsami.8b17636.
[79] T.K. Chang, Y.C. Lu, S.T. Yeh, T.C. Lin, C.H. Huang, C.H. Huang, In vitro and in vivo biological responses to graphene and graphene oxide: a murine calvarial animal study, Int. J. Nanomed. 15 (2020) 647–659, https://doi.org/10.2147/ijn.S231885.
[80] M. Makita, K. Yamakado, A. Nakatsuka, H. Takaki, T. Inaba, F. Oshima, H. Katayama, K. Takeda, Effects of barium concentration on the radiopacity and biomechanics of bone cement: experimental study, Radiat. Med. 26 (9) (2008) 533–538, https://doi.org/10.1007/s11604-008-0269-0.
[81] N. Kobayashi, D. Togawa, T. Fujishiro, K.A. Powell, A.S. Turner, H.B. Seim 3rd, T.W. Bauer, Histological and radiographic evaluation of polymethylmethacrylate with two different concentrations of barium sulfate in a sheep vertebroplasty model, J. Biomed. Mater. Res. 75 (1) (2005) 123–127, https://doi.org/10.1002/jbm.a.30388.
[82] M. Khandaker, M.B. Vaughan, T.L. Morris, J.J. White, Z. Meng, Effect of additive particles on mechanical, thermal, and cell functioning properties of poly(methyl methacrylate) cement, Int. J. Nanomed. 9 (2014) 2699–2712, https://doi.org/10.2147/ijn.S61964.
[83] S.M. Kurtz, M.L. Villarraga, K. Zhao, A.A. Edidin, Static and fatigue mechanical behavior of bone cement with elevated barium sulfate content for treatment of vertebral compression fractures, Biomaterials 26 (17) (2005) 3699–3712, https://doi.org/10.1016/j.biomaterials.2004.09.055.
[84] N. Shearwood-Porter, M. Browne, I. Sinclair, Micromechanical characterisation of failure in acrylic bone cement: the effect of barium sulphate agglomerates, J. Mech. Behav. Biomed. Mater. 13 (2012) 85–92, https://doi.org/10.1016/j.jmbbm.2012.04.012.
[85] M.D. Lazarus, J.M. Cuckler, H.R. Schumacher Jr., P. Ducheyne, D.G. Baker, Comparison of the inflammatory response to particulate polymethylmethacrylate debris with and without barium sulfate, J. Orthop. Res. : official publication of the Orthopaedic Research Society 12 (4) (1994) 532–541, https://doi.org/10.1002/jor.1100120410.
[86] E. Ingham, T.R. Green, M.H. Stone, R. Kowalski, N. Watkins, J. Fisher, Production of TNF-alpha and bone resorbing activity by macrophages in response to different types of bone cement particles, Biomaterials 21 (10) (2000) 1005–1013, https://doi.org/10.1016/s0142-9612(99)00261-6.
[87] D. Togawa, T.W. Bauer, I.H. Lieberman, S. Takikawa, Histologic evaluation of human vertebral bodies after vertebral augmentation with polymethyl methacrylate, Spine 28 (14) (2003) 1521–1527.
[88] C.I. Vallo, P.E. Montemartini, M.A. Fanovich, J.M. Porto López, T.R. Cuadrado, Polymethylmethacrylate-based bone cement modified with hydroxyapatite, J. Biomed. Mater. Res. 48 (2) (1999) 150–158, https://doi.org/10.1002/(sici)1097-4636(1999)48:2<150::aid-jbm9>3.0.co;2-d.